

# Investigating the surface process response to fault interaction and linkage using a numerical modelling approach

P. A. Cowie,\* M. Attal,\* G. E. Tucker,† A. C. Whittaker,\* M. Naylor,\* A. Ganas‡ and G. P. Roberts§

\**Institute of Earth Science, School of GeoSciences, Edinburgh University, Edinburgh, UK*

†*Cooperative Institute for Research in Environmental Sciences (CIRES) and Department of Geological Sciences, University of Colorado, Boulder, CO, USA*

‡*Institute of Geodynamics, National Observatory of Athens, Thission, Athens, Greece*

§*Research School of Geological and Geophysical Sciences, Birkbeck College and University College London, London, UK*

## ABSTRACT

In order to better understand the evolution of rift-related topography and sedimentation, we present the results of a numerical modelling study in which elevation changes generated by extensional fault propagation, interaction and linkage are used to drive a landscape evolution model. Drainage network development, landsliding and sediment accumulation in response to faulting are calculated using CASCADE, a numerical model developed by Braun and Sambridge, and the results are compared with field examples. We first show theoretically how the ‘fluvial length scale’,  $L_f$ , in the fluvial incision algorithm can be related to the erodibility of the substrate and can be varied to mimic a range of river behaviour between detachment-limited (DL) and transport-limited (TL) end-member models for river incision. We also present new hydraulic geometry data from an extensional setting which show that channel width does not scale with drainage area where a channel incises through an area of active footwall uplift. We include this information in the coupled model, initially for a single value of  $L_f$ , and use it to demonstrate how fault interaction controls the location of the main drainage divide and thus the size of the footwall catchments that develop along an evolving basin-bounding normal fault. We show how erosion by landsliding and fluvial incision varies as the footwall area grows and quantify the volume, source area, and timing of sediment input to the hanging-wall basin through time. We also demonstrate how fault growth imposes a geometrical control on the scaling of river discharge with downstream distance within the footwall catchments, thus influencing the incision rate of rivers that drain into the hanging-wall basin. Whether these rivers continue to flow into the basin after the basin-bounding fault becomes fully linked strongly depends on the value of  $L_f$ . We show that such rivers are more likely to maintain their course if they are close to the TL end member (small  $L_f$ ); as a river becomes progressively more under supplied, i.e. the DL end member (large  $L_f$ ), it is more likely to be deflected or dammed by the growing fault. These model results are compared quantitatively with real drainage networks from mainland Greece, the Italian Apennines and eastern California. Finally, we infer the calibre of sediments entering the hanging-wall basin by integrating measurements of erosion rate across the growing footwall with the variation in surface processes in space and time. Combining this information with the observed structural control of sediment entry points into individual hanging-wall depocentres we develop a greater understanding of facies changes associated with the rift-initiation to rift-climax transition previously recognised in syn-rift stratigraphy.

## INTRODUCTION

Fault growth is widely recognised as an important factor influencing the geometry of drainage networks and the direction of surface flow into and within active rift basins (e.g. Burbank & Anderson, 2001). Previous studies have highlighted in particular the importance of fault segmentation in controlling the location, size and shape of foot-

Correspondence: P. A. Cowie, Institute of Earth Science, School of GeoSciences, Kings Buildings, Edinburgh University, West Mains Road, Edinburgh EH9 3JW, UK. E-mail: Patience.Cowie@ed.ac.uk.

wall catchments and the focussing of sediment supply to hanging-wall depocentres (e.g. Roberts & Jackson, 1990; Gawthorpe & Hurst, 1993; Leeder & Jackson, 1993; Eliet & Gawthorpe, 1995; Gupta *et al.*, 1999; Jackson *et al.*, 2002). These studies document many field examples but they rarely provide a quantitative process-based explanation for specific geomorphic phenomena. To fully interpret the significance of the geomorphic features observed in areas of active extension, and to predict variations in sediment supply to rift basins through time, we need to consider explicitly the timing and rates of fault growth as well as the nature and rates of surface processes (e.g. Densmore *et al.*, 1998; Allen & Densmore, 2000; Hardy & Gawthorpe, 2002; Carretier & Lucazeau 2005; see van der Beek *et al.* (2002) and Tucker & Slingerland (1996) for studies in compressional settings). Densmore *et al.* (2003) demonstrated this point explicitly via numerical modelling of landscape evolution at a relay zone between two actively growing extensional fault segments. They varied the rate of fault tip propagation on the two adjacent fault segments and showed quantitatively that the rate of propagation directly influenced the size and location of drainage basins within the footwall and relay zone areas as well as the sediment volume delivered to depocentres on the hanging-wall side of the fault. However, the tectonic forcing in their model consists of two straight faults with a smooth variation of displacement along fault strike; the rate of fault propagation in each model run is constant and prescribed. On the other hand, previous modelling approaches that have included temporal variations in fault slip rate have ignored the along-strike variations in fault displacement associated with segmentation (Allen & Densmore, 2000; Hardy & Gawthorpe, 2002).

In this paper we seek a deeper understanding of how normal-fault growth patterns drive the evolution of drainage networks, topography and basin depocentres. We present results from a numerical modelling study that uses a surface process model coupled to a model of normal-fault growth in which spatial variations in fault displacement *and* temporal variations in fault slip rate emerge spontaneously as the deformation proceeds. Note that this is a one-way coupled model, i.e. there is no influence of the erosion on the tectonic evolution. The variations in fault growth rate result from stress interactions between adjacent active fault segments. Fault interaction via perturbation to the regional stress field is a fundamental feature of the way that fault arrays evolve within the brittle crust. By coupling the tectonic model with a surface process model we provide an unprecedented opportunity to study the dynamic interplay between fluvial incision and landsliding in response to this actively evolving 3D uplift field on a regional scale. Both the surface process model and the tectonic model have been described extensively in previous papers as separate modelling approaches (see 'The tectonic model' and 'The surface process model' below). This paper focuses instead on the coupled model and thereby derives new insights into landscape evolution and sediment supply variations in response to normal-fault growth.

The key tectonic process that we focus on in this paper is the evolution through time from a diffuse array of unconnected extensional fault segments to the formation of a major through-going basin-bounding fault and the changes in slip rate that accompany this spatial organisation of the fault pattern. The creation of hanging-wall accommodation associated with this structural evolution has previously been discussed by Gupta *et al.* (1998) and Cowie *et al.* (2000), but the potential for spatial and temporal variations in sediment supply to the growing depocentres was not considered. Specific questions that we address in this study concern the temporal evolution of drainage patterns in response to the growing normal faults over several million years. For example, what does the drainage network geometry imply about the relative timing and rate of fault slip on adjacent interacting fault segments? What fundamentally determines the incision rate of rivers that drain across an actively uplifting and back-tilting footwall block? More generally, are large drainages that incise across areas of footwall uplift necessarily antecedent, i.e. existed before the onset of extension? How does the evolution of the fault array influence the location of the main drainage divide relative to the rift basin margin? And what are the implications of the drainage network evolution within the uplifted footwall for sediment supply and dispersal to the adjacent hanging-wall depocentres? We investigate these issues via numerical simulation using a generic but realistic history of fault development. In the Discussion we compare the model results with specific field examples. We also re-evaluate the interpretation of syn-rift stratigraphic patterns from the perspective of catchment development and surface processes occurring within the uplifted footwall (or 'rift shoulder') that borders a developing extensional basin.

## THE TECTONIC MODEL

The tectonic model used here is based on well-established concepts of stress enhancement and shadowing around active, seismogenic faults (Cowie *et al.*, 1993; Cowie, 1998). It allows us to simulate the spontaneous evolution through time of a population of faults, each of which perturbs the surrounding stress field and thereby interacts with neighbouring faults. The model is described in detail by Cowie *et al.* (1993), Sornette *et al.* (1994) and Cowie (1998). It consists of a thin elastic-brittle plate represented by a 2D square lattice, across which we impose antiplane shear deformation. The lattice is made up of  $180 \times 180$  elements that are oriented at  $45^\circ$  to the plate edges. Cyclic boundary conditions are applied in the  $x$ -direction (Fig. 1). A uniform antiplane shear strain is imposed across the lattice by applying increments of stress to all the elements throughout the lattice at each model time step. This is equivalent to a constant strain rate boundary condition which drives the deformation. Material strength is heterogeneous across the model and has a fixed, uniformly random, distribution. When an element ruptures, it un-

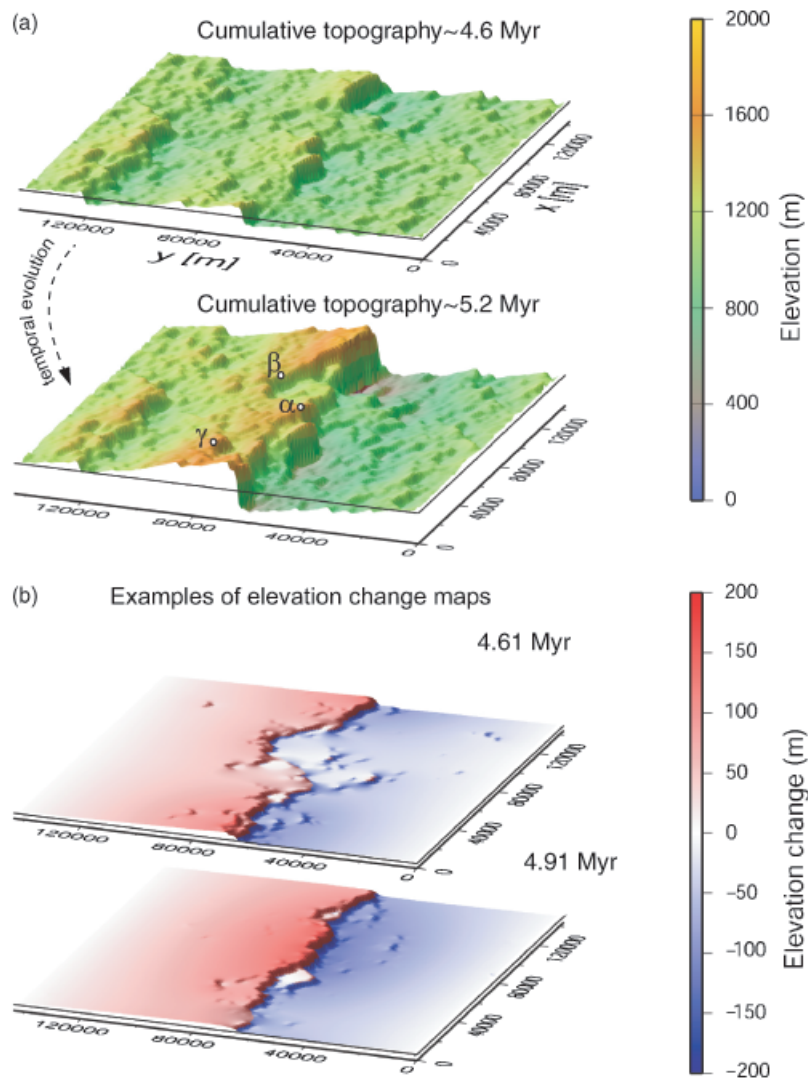


Fig. 1. (a) Examples of topography extracted from the tectonic model for extensional fault growth. Note the approximately bi-modal distribution of surface slope, i.e. shallow dip slopes (few degrees) in the footwall and hanging-wall areas and sub-vertical slopes on the fault scarps. Points  $\alpha$ ,  $\beta$ ,  $\gamma$  refer to locations where fault throw has been calculated and plotted in Fig. 2. (b). Examples of two maps of incremental elevation change due to fault slip extracted from the tectonic model (at 4.61 Myr (top) and 4.91 Myr (bottom) in these examples) and used as input in surface process model (see 'Coupling the tectonic and surface process models' for explanation of model coupling).

dergoes an instantaneous stress drop and the model calculates and stores the amount of permanent shear displacement necessary to drop the stress at that point. The stress field throughout the lattice is recalculated after each individual rupture. Ruptured elements heal instantaneously and thus can accumulate further stress and may re-rupture many times during a simulation. Note that there is no actual change in the length of lattice elements.

The raw output of the model is a continuous deformation field across the 2D lattice, which consists of elastic deformations plus, where elements have ruptured, vertical shear dislocations. We impose a rigid-body rotation proportional to the total shear strain across the lattice to produce tectonic topography comparable to tilted fault blocks, as described in Cowie *et al.* (2000). Figure 1 shows examples of the tectonic topography at two different time periods during the evolution, compared with incremental eleva-

tion changes at two intervening points in time. The main characteristics of the fault evolution that provides the tectonic forcing for the coupled model are summarised in Fig. 2, which shows data extracted from Fig. 1. Before 2.5 Myr the deformation is dominated by nucleation of new faults with limited interaction. At  $\sim 2.5$  Myr fault interaction becomes important and the rates of fault nucleation and fault 'death' due to stress shadowing are approximately in balance. During this phase the slip rates on the faults are very variable in space and time but generally very low. By 3.8 Myr the interaction between neighbouring faults becomes significant and the number of active faults begins to decline (Fig. 2b). Between 4.6 and 5.2 Myr, strong elastic interaction and fault segment linkage dominate the deformation. During this interval most of the activity is concentrated along a single fault extending across the centre of the model space (at  $y \approx 65$  km; Fig. 1)

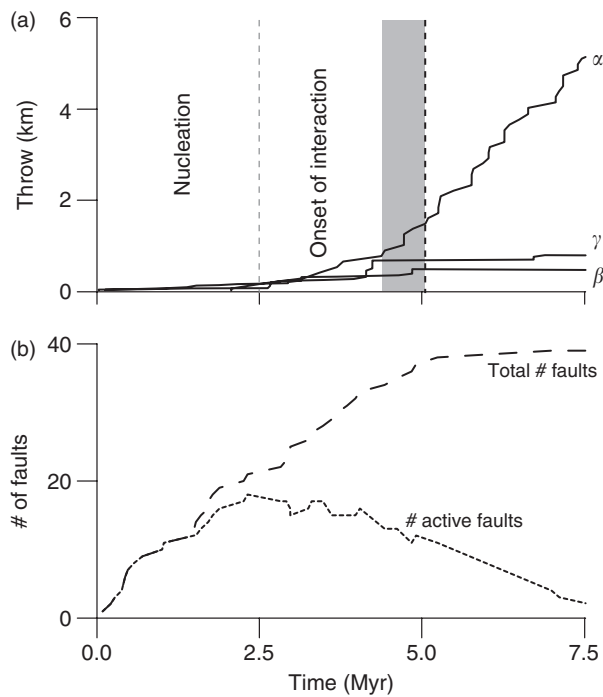


Fig. 2. (a) Throw vs. time for faults at locations  $\alpha$ ,  $\beta$  and  $\gamma$  (see Fig. 1) and (b) fault activity for the tectonic model used in this study. Grey shading indicates time period of strong fault interaction and linkage. Vertical black dashed line indicates time (i.e. 5.2 Myr) at which fault array becomes linked across entire width of model. The total number of faults is derived by applying a clustering algorithm to the pattern of ruptured lattice elements; active faults are defined as a cluster that has ruptured in the last time-step.

and the fault slip rate on this fault begins to increase (e.g. fault ' $\alpha$ '; Figs 1 and 2a). Constant strain rate overall is maintained because many early-formed faults have become inactive by this time because they now lie in the stress shadow of a larger structure (faults ' $\beta$ ' and ' $\gamma$ '; Fig. 2b). The fault array is connected continuously for the first time from one side of the lattice to the other by 5.2 Myr, although there are still significant variations in displacement along its length at this time. Note that the average slip rate on the linked fault is  $\sim 1 \text{ mm yr}^{-1}$ , i.e. significantly higher than before 4.6 Myr when the rates are  $< 0.4 \text{ mm yr}^{-1}$ .

The details of how the model is scaled to produce a physically realistic faulted topography are described in full by Cowie *et al.* (2000). In the simulations shown here the model scaling was chosen such that our results may be compared with active extensional settings worldwide that are characterised by high-angle normal faulting (e.g. East African Rift, Basin and Range, mainland Greece and the Italian Apennines). The spacing between the lattice nodes in both the  $x$ - and  $y$ -directions is set equal to 800 m and each increment of shear offset on a ruptured element is multiplied by 80 m to obtain fault displacements in meters. This yields a model that is  $144 \times 144 \text{ km}$  in terms of total area, maximum fault displacements of a few kilometres and maximum fault segment lengths of 30–40 km. With this model scaling the maximum angle of tilt on the

hanging-wall and footwall dip slopes due to the imposed rotation is a few degrees and the fault plane dips remain  $> 60^\circ$ .

### Does this tectonic model produce realistic patterns of normal-fault evolution?

The stress perturbation associated with rupture of a single element in this model is comparable to that for a steeply dipping ( $> 60^\circ$ ) normal fault in an elastic medium, i.e. regions of stress increase along strike from the rupture zone and regions of stress shadow in the transverse direction (Cowie *et al.*, 1993, 2000; Cowie, 1998). This pattern favours the development of en échelon or coplanar fault arrays which are so characteristic of extensional provinces. Using this model, Cowie (1998) showed that the onset of more rapid along-strike fault growth and, ultimately, segment linkage is due to elastic interaction between neighbouring fault segments and is associated with an increase in slip rate on the linking fault array. It is balanced by a contemporaneous cessation of activity (or declining slip rate) on structures that lie in the stress shadow zones of the linking array such that constant strain rate is maintained overall when the entire fault population is considered (Gupta *et al.*, 1998; Roberts *et al.*, 2002).

Gupta *et al.* (1998) and Cowie *et al.* (2000) describe a number of examples from rift basins that are consistent with this tectonic model. In these examples the accumulation of bio-stratigraphically dated sediments adjacent to the evolving faults provides a 'tape-recorder' of fault activity and growth. Using these examples it can be shown that the onset of more rapid basin deepening and the formation of major extensional fault systems with increased rates of slip coincide with the abandonment of many smaller scale faults within the basin (e.g. Contreras *et al.*, 2000; McLeod *et al.*, 2000; Sharp *et al.*, 2000; Cowie & Roberts, 2001; Roberts *et al.*, 2002; Gawthorpe *et al.*, 2003). Moreover, Taylor *et al.* (2004) and McLeod *et al.* (2000) show that the increase in slip rate coincides, within error, to the timing of fault linkage in the areas they studied. In all these examples the increase in fault slip rate is not explained by an overall increase in basin extension rate but can be attributed instead to the cessation of activity on a large number of small-scale faults. The significance of this transition in structural style for the present study is that as the degree of along-strike continuity of the fault scarp changes, the rate of footwall uplift, and thus structural relief across the fault, increases.

Elastic interaction between growing faults also leads to episodic fault slip (e.g. Fig. 2a). There is an increasing body of literature that presents field evidence for non-uniform moment release rate on faults over geologic time (e.g. Rockwell *et al.*, 2000; Friedrich *et al.*, 2003; Palumbo *et al.*, 2004; Chevalier *et al.*, 2005; Bull *et al.*, 2006). However, the time scales of the episodicity and the magnitude of the variability of the fault slip rates are generally not well constrained (cf. Mortimer *et al.*, 2005; Bull *et al.*, 2006). In the tectonic model we use here the fault displacement accu-

mulation curves show a distinctively episodic character, with slip rates varying from  $\sim 0 \text{ mm yr}^{-1}$  to several  $\text{mm yr}^{-1}$  over time periods ranging from  $10^4$  to  $10^5$  years (Fig. 2). The episodic nature of fault movement becomes important for modelling and interpreting the transient response of the landscape when the timescale of the episodicity is comparable to the timescale of erosional processes (see 'Influence of varying  $L_f$ ' and 'Controls on fluvial incision across growing footwall uplifts').

### Coupling the tectonic and surface process models

The topography that is generated by the tectonic model is stored every 100 rupture events and then used to construct a series of maps of tectonic elevation change (e.g. Fig. 1b). These maps are read sequentially as input files to the surface process model. Because this is a one-way coupled model, there is no influence of the erosion on the tectonic evolution. A fully coupled model is beyond the scope of the present study. The total time of the coupled simulation is 6 Myr but we focus on the evolution of topography for the interval 2.5–6 Myr, which encompasses the main phase of fault interaction and linkage between 4.6 and 5.2 Myr (Fig. 2). For the 3.5 Myr interval of fault growth of interest we extracted 125 maps of tectonic elevation change with an average time interval per map of 28 000 years (e.g. Fig. 1b). The evolution before 2.5 Myr is calculated by linearly interpolating between a flat surface and the tectonic topography at 2.5 Myr. The surface process model uses a dynamic time step that is generally at least two orders of magnitude shorter (e.g.  $\sim 100$  years) than the time interval between the tectonic maps. Thus the surface process model linearly interpolates between maps to obtain the elevation change proportionate to each (dynamic) time step. As a result of the linear interpolation, we ensure that the maximum elevation change that occurs due to fault movement in a single time step of the surface process calculations is  $< 1 \text{ m}$  and the maximum slip rate on individual fault scarps is of the order of a few  $\text{mm yr}^{-1}$ . These values are comparable to elevation changes associated with single earthquakes and slip rate estimates for real extensional faults. Note that the interpolation procedure does not suppress the episodic nature of fault activity seen in the tectonic model, as this is an important aspect of our study. We do not include any pre-existing (i.e. pre-fault growth) topography in this model. Consequently, the initial drainage pattern has a strong imprint from the early phases of fault growth and no 'inheritance' from prior topography. All the model runs presented in this paper use the same tectonic forcing (i.e. Fig. 1) as the input to the coupled model with the exception of the experiments shown in Figs 9(b) and 15(b).

### THE SURFACE PROCESS MODEL

We use the surface process model developed originally by Beaumont *et al.* (1992) and later modified and elaborated by

Braun & Sambridge (1997), van der Beek & Braun (1998) and Champel *et al.* (2002). The numerical code is called CASCADE and it models fluvial erosion, diffusive hill-slope processes, sediment deposition and landsliding (following the approach of Densmore *et al.*, 1998). Lake development is modelled as instantaneous filling to the lowest point on the catchment boundary (i.e. the sill or pour point). The grid geometry used in CASCADE corresponds exactly to the original lattice geometry of the tectonic model and this geometry is fixed through time. Each cell in CASCADE is diamond shaped, because of the  $45^\circ$  lattice geometry (see 'The tectonic model'), with a side length  $dx = \sqrt{2} \times 800$ , aspect ratio = 1 and grid nodes located at each apex. Thus the surface area of each diamond-shaped cell is  $1600 \text{ m} \times 800 \text{ m} = 1.28 \times 10^6 \text{ m}^2 = 1.28 \text{ km}^2$  and the total area of the model is  $144 \times 144 \text{ km}$ . There is no channel initiation threshold so every cell can erode (or aggrade) by fluvial processes in addition to the other processes of mass movement. The algorithm used in CASCADE for modelling landslides is described in Champel *et al.* (2002) with the slope for landslide initiation set to  $21^\circ$ . Hill-slope diffusion is considered negligible at the resolution of the model used in this study. Finally, all material is assumed here to have a homogeneous, uniform erodability. Table 1 summarises the model parameters used in this study.

A key feature of this study is the so-called 'under-capacity' model for fluvial incision and transport that is used within CASCADE. Several other models have been proposed (e.g. Whipple & Tucker, 2002), but at present there is not a strong empirical basis for choosing among them. Furthermore, the 'under-capacity' model is able to mimic the behaviour of other river incision models by varying the fluvial length-scale parameter,  $L_f$ , as we review below (see also van der Beek & Braun, 1998; van der Beek & Bishop,

**Table 1.** Summary of model parameters used in the study

Parameter	Definition	Units	Value
$h$	Elevation	m	
$U$	Uplift rate	$\text{m s}^{-1}$	
$W$	Channel width	m	10
$Q$	Volumetric river discharge	$\text{m}^3$	
$q$	Discharge/unit width	$\text{m}^2 \text{ s}^{-1}$	
$A$	Drainage area	$\text{m}^2$	
$S$	Channel slope		
$S_0$	Initial channel slope		
$v$	Effective precipitation rate	$\text{m s}^{-1}$	1
$Q_s$	Volumetric sediment flux	$\text{m}^3 \text{ s}^{-1}$	
$q_s$	Sediment flux/unit width	$\text{m}^2 \text{ s}^{-1}$	
$Q_c$	Volumetric transport capacity	$\text{m}^3 \text{ s}^{-1}$	
$q_c$	Transport capacity/unit width	$\text{m}^2 \text{ s}^{-1}$	
$L_f$	Fluvial length scale	m	10.0E4–10.0E5
$K_f$	Dimensionless transport parameter		5.00E–02
$D$	Detachment rate	$\text{m s}^{-1}$	
$D_c$	Detachment capacity	$\text{m s}^{-1}$	
$\phi$	Scaling exponent in $W \propto Q^\phi$		0–0.5

2003). We believe that the results presented here are generic enough that similar findings would be obtained with other models and, moreover, that it is instructive to study the full spectrum of behaviour that lies between the end members of transport limited (TL) and detachment limited (DL) conditions.

According to the revised formulation of this model (van der Beek & Bishop, 2003) incision rate,  $dh/dt$  is given by

$$\frac{dh}{dt} = \frac{1}{WL_f}(Q_c - Q_s). \quad (1)$$

In Eqn. (1),  $W$  is channel width,  $Q_s$  is volumetric sediment flux, and  $Q_c$  is the transport capacity of the river given by

$$Q_c = K_f vAS \quad (2)$$

where  $K_f$  is a dimensionless fluvial transport capacity parameter,  $v$  is effective precipitation rate (constant across the model),  $A$  is total upstream drainage area and  $S$  is channel bed slope. Furthermore, because  $v$  is uniform in space and time, river discharge  $Q = vA$ . Potential inaccuracies arising from this assumption are discussed by Solyom & Tucker (2004).

The volumetric sediment flux,  $Q_s$ , is obtained by performing a mass balance calculation at each downstream position  $R$ , i.e.

$$Q_s|_{\vec{r}=R} = \int_0^A \frac{dh}{dt} da$$

where  $\vec{r}$  is streamwise distance downstream from the source and  $a$  is drainage area. Sedimentation occurs whenever  $Q_s > Q_c$  and consequently there is sediment accumulation in the basins on the hanging-wall side of the fault scarps. However, the basins are underfilled in our study because of the finite dimensions of the model. In real rift basins there is usually a significant contribution to basin fill transported axially into the depocentres from other regions in addition to that derived from the adjacent footwall. To try and incorporate this externally derived contribution would have involved additional arbitrary assumptions which we wished to avoid. The magnitude of base-level fall along the faults is larger than it would be if the basins were in-filled but this aspect of the model does not affect our overall conclusions.

### Morphologic significance of $L_f$

In this paper we vary the parameter  $L_f$  (Eqn. (1)) in order to investigate its influence on the development of the drainage network in response to fault growth. It is important to first review the physical interpretation of this parameter and to explain theoretically its morphologic impact. In Appendix A we demonstrate that  $L_f$  can be interpreted as a measure of relative erodability of the substrate, i.e.  $L_f = q_c/D_c$ , where  $D_c$  is the clear-water detachment capacity of the flow and  $q_c$  is sediment transport capacity per unit flow

width (Eqns (A.4) and (A.5)). This expression for  $L_f$  assumes that the threshold value for the onset of particle entrainment is effectively zero (see Appendix A), implying that the bedrock of the channel contains some fraction (possibly small) of friable material that is readily entrained (cf. Tucker, 2004). High values of  $L_f$  represent the case of a more resistant lithology such that  $q_c \gg D_c$  and the river is strongly under-capacity ( $Q_s \ll Q_c$ ). Conversely, low values of  $L_f$  represent rocks that are highly erodible, so that  $q_c \ll D_c$  and the river approaches its equilibrium carrying capacity ( $Q_s \approx Q_c$ ). Note that material derived from landsliding is treated as bedrock in CASCADE and does not constitute a source of sediment in the fluvial incision algorithm (see Champel *et al.*, 2002).

In varying  $L_f$  we first of all note that the intrinsic concavity of the river profiles (*sensu* Whipple & Tucker, 1999) will vary and this directly impacts the resulting 3D morphology of the eroded landscape, as shown by Tucker & Whipple (2002). The dependence of intrinsic concavity on  $L_f$  is most easily demonstrated by considering the case of constant incision rate equal to an uplift rate,  $U$ . If we assume  $Q_s = UAb$ , where  $b$  represents the fraction of the sediment load that exerts the main control on the channel gradient ( $b \leq 1$ ), then from Eqns (1) and (2) we obtain

$$S = \frac{U}{K_f v} \left( b + \frac{WL_f}{A} \right). \quad (3)$$

Thus, when  $L_f$  is small  $(WL_f)/A$  becomes negligible, giving  $S \approx \text{constant}$  (zero concavity) and the resulting landscape will be relatively smooth with open valleys and approximately linear stream networks (e.g. see Fig 2a in Whipple & Tucker (2002)). Conversely, when  $L_f$  is large,  $S \propto A^{-1}$ , i.e. a concavity of 1, resulting in topography that is much rougher, with deep valleys and tortuous drainage networks (e.g. see Fig. 2c in Whipple & Tucker (2002)). Although this calculation is based on the assumption of topographic steady state it remains a helpful way to understand how varying  $L_f$  may influence our results.

Varying  $L_f$  also determines the response of the river to sudden base-level fall such as that generated by the movement of an active fault. As  $L_f$  becomes very large,  $Q_s \rightarrow 0$  and Eqn. (1) becomes

$$\frac{dh}{dt} \propto Q \frac{dh}{dx}, \quad \frac{dh}{dx} < 0 \quad (4)$$

where channel slope  $S = |(dh/dx)|$  and  $Q = vA$ . Equation (4) has the form of a wave equation and it describes one 'end-member' incision model in which the detachment capacity of the river is the limiting control on incision rate (Whipple & Tucker, 1999). The velocity of the wave in this case equals  $(QK_f)/(WL_f)$ . Conversely, in the limit that  $L_f$  is infinitesimally small, an advection-diffusion equation describing TL river incision is obtained:

$$\frac{dh}{dt} \propto \frac{d}{dx} \left( Q \frac{dh}{dx} \right). \quad (5)$$

This is the other 'end-member' incision model in which the finite transport capacity of the river is the dominant control on incision rate. As Whipple & Tucker (2002) have already shown, the transient responses of TL and DL systems are quite distinct: TL systems are characterised by diffusive gradual changes in channel gradient whereas DL systems are characterised by the upstream migration of an abrupt knickpoint.

In general, for  $L_f > dx$  ( $dx$  = node spacing in the numerical model) the river is 'under-capacity', i.e.  $0 < Q_s < Q_c$  and the incision rate depends on the magnitude of  $(Q_c - Q_s)$ . Thus the role of sediment in this model is to shield the river bed rather than to enhance abrasion and plucking by the impact of sediment particles on the channel base (cf. Sklar & Dietrich, 1998, 2004). Consequently, rivers carrying a large sediment load relative to transport capacity are, in theory, less able to incise according to this model (the 'linear decline model' referred to by Whipple & Tucker, 2002). However, the only changes in  $Q_s$  in this model are driven by the incision algorithm (Eqn. (1)) and there is a trade-off between the value of  $L_f$  and the relative under-capacity of the river ( $Q_c - Q_s$ ). Thus the steady-state incision rate of a river with small  $L_f$  and  $Q_s \approx Q_c$  is not actually less than that of a river with large  $L_f$  and  $Q_s \ll Q_c$ . What is of key importance in this study is the length scale over which local perturbations to the steady-state ratio  $Q_s/Q_c$  will persist; in particular, those changes in  $Q_c$  due to tectonic tilting and/or base-level changes associated with fault slip. In Appendix A we demonstrate that  $L_f$  can also be interpreted as the distance over which, for constant  $q_c$  and  $D_c$ , the ratio  $Q_s/Q_c$  increases by  $1k$  (Eqn. (A.3)). Thus, when  $L_f \rightarrow dx$  any local increase in  $Q_c$  due to fault movement will be instantaneously matched by incision to re-establish the condition  $Q_s \approx Q_c$  at that point. In contrast, when  $L_f$  is large the incision response to the same magnitude change in  $Q_c$  will be negligible unless the change in  $Q_c$  is very big. It is this difference in the persistence of a perturbation within the fluvial system that underlies the contrasting 'end-member' behaviours described by Eqns (4) and (5) above. It is clear therefore that  $L_f$  fundamentally determines the response of the fluvial network to fault activity and is a key component in our understanding of the coupled system. In this study we are not restricted to the end-member cases but can investigate the full spectrum of behaviour by varying  $L_f$  ('Influence of varying  $L_f$ ').

### Hydraulic geometry – channel width, $W$

In previous applications of the under-capacity model (e.g. Beaumont *et al.*, 1992; Kooi & Beaumont, 1996; van der Beek & Braun, 1998; Champel *et al.*, 2002) channel width is assumed to be constant, implying that incision rate is a function of stream power per unit length and is independent of hydraulic geometry. Although this assumption might be appropriate in some settings (e.g. Seidl & Dietrich, 1992), it is important that we re-examine it within this study. Many other landscape evolution models assume that incision rate is a function of stream power (or shear

stress) per unit bed area and therefore does depend on hydraulic geometry. Typically, it is also assumed that channel width  $W \propto Q^{0.5}$ , where  $Q$  is river discharge. This scaling relationship is well-established for low gradient alluvial rivers where the channel banks are easily modified in response to changes in channel flow (e.g. Leopold & Maddock, 1953). Tucker & Whipple (2002) show that erosion models which incorporate this scaling between  $W$  and  $Q$  can reproduce realistic steady-state topography and river profile concavity. Similar scaling relationships,  $W \propto Q^{0.35-0.5}$ , have been established for bedrock channels where there are no significant variations in bedrock erodability or localised tectonic disturbance of the channel (Snyder *et al.*, 2000, 2003; Montgomery & Gran, 2001; Duvall *et al.*, 2004).

The present study is concerned with the surface process response to a dynamically evolving fault array so the system may not achieve steady state. Moreover, strong local disturbance of river channels occurs where they drain across active faults. Thus, whilst we accept that  $W \propto Q^{0.5}$  may best describe the globally averaged variation in channel width, it is not necessarily appropriate to assume it *a priori*. For example, Finnegan *et al.* (2005) argue that for areas with spatially non-uniform rock uplift rates, channel width must depend on channel slope,  $S$ , as well as  $Q$ . They assume that channel aspect ratio and roughness are constant for a given rock type in order to derive a modified scaling relationship, i.e.  $W \sim Q^{0.38} S^{-0.19}$ . This relationship provides a significantly better fit to channel width measurements for a river draining across an antiformal uplift in southeast Tibet than can be obtained by using  $W \propto Q^{0.5}$ . However, there are published examples of rivers draining across active thrust faults where this relationship clearly does not explain the observations, e.g. Harbor (1998) and Lavé & Avouac (2001). In these cases, significant changes in channel width (or active flood plain width (Lavé & Avouac (2001)) occur that do not correlate with convex reaches. The reason the model of Finnegan *et al.* (2005) is unable to account for all cases is that it is empirically based and rests fundamentally on assumptions of steady-state channel geometry.

It is clear from the above discussion that assuming an empirical scaling relationship such as  $W \propto Q^{0.5}$  is inappropriate for this study while modelling the evolution of  $W$  explicitly is beyond the scope of the present work. We therefore rely on field measurements of channel width along a river that crosses an active normal fault, the Fiamignano fault, in central Italy (Fig. 3). The fault is  $\sim 25$  km in length and the Rio Torto crosses the fault near its centre where the throw is  $\sim 1.8$  km and the throw rate is  $\sim 1$  mm yr<sup>-1</sup>. The drainage basin extends over a significant proportion of the back-tilting footwall and the throw and throw rate vary along fault strike (Fig. 3a). The rock uplift rate is therefore non-uniform across the entire 65 km<sup>2</sup> catchment of this river. Whittaker *et al.* (in press) present a detailed field study of the Rio Torto in which they quantify high flow channel width and Selby rock mass strength variations downstream. The convex long profile indicates that

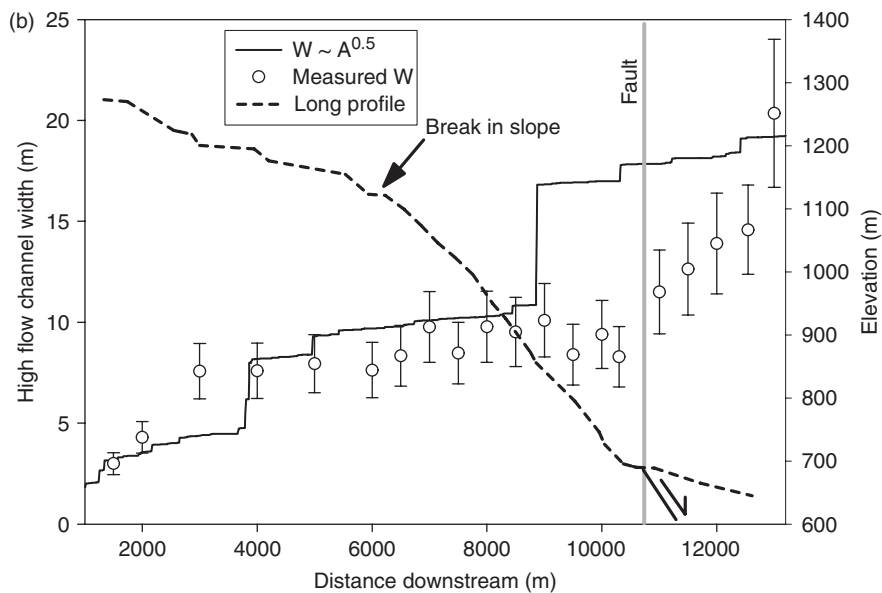
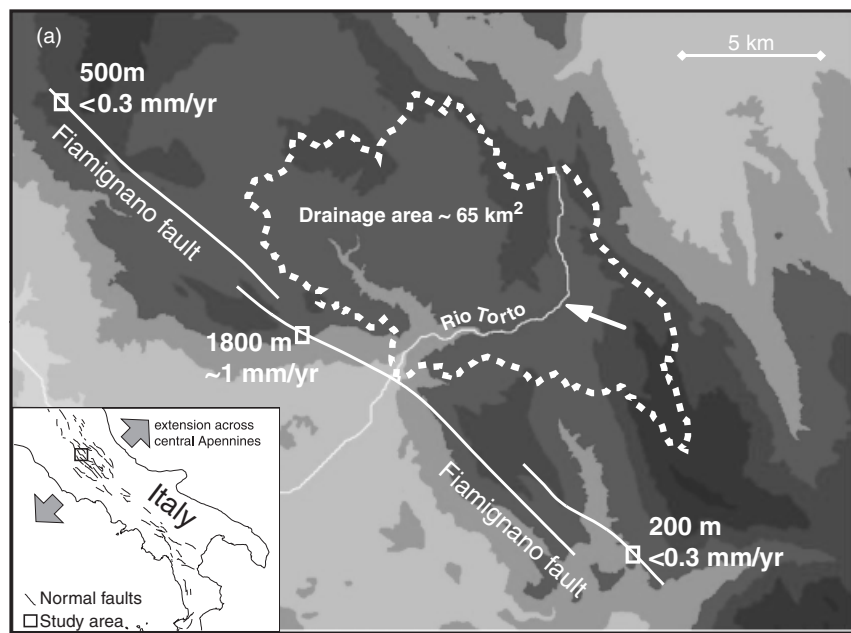


**Fig. 3.** (a) Location map of the Rio Torto draining from the footwall into the hanging wall of an active normal fault, the Fiamignano fault, in central Italy (modified from Whittaker *et al.*, in press). The watershed for this catchment is shown by the white dashed line. White arrow marks the top of the convex reach of the river upstream of the fault. Squares mark points where total throw (top value) and throw rate (bottom value) have been estimated. Where the river crosses the fault the total throw is  $\sim 1.8$  km and the slip rate is  $\sim 1$  mm yr $^{-1}$  but the throw and throw rate vary along strike. (b) High flow channel width,  $W$  (dots) measured every 20–30 m downstream and channel bed elevation extracted from a 20 m DEM (dashed line), as a function of distance measured along the Rio Torto, upstream of the Fiamignano fault. Width data are averaged over 500 m intervals to obtain the mean and standard deviation for each reach. The solid line in (b) is the empirical relationship  $W \propto Q^{0.5}$ , assuming  $Q \propto A$  where  $A$  is drainage area. Black arrow in (b) marks the top of the convex reach upstream of the fault. See ‘Hydraulic geometry – channel width,  $W$ ’ for discussion.

this system is not in equilibrium with respect to the rate of energy dissipation downstream and is unlikely to be in steady state (Whittaker *et al.*, in press). The convexity does not correlate with changes in bedrock lithology or rock mass strength (Whittaker *et al.*, in press). More importantly, the data shown in Fig. 3b reveal that high flow channel width is approximately uniform for a significant

portion of the river upstream of the fault and that changes in drainage area are not mirrored by changes in channel width. In the light of the arguments and data presented here we therefore make the assumption that  $W$  is constant and in ‘Controls on fluvial incision across footwall uplifts’ we discuss the impact of this assumption on our results.

## RESULTS DERIVED FROM THE COUPLED MODEL

In this paper we primarily investigate the influence of varying the parameter  $L_f$ . This parameter determines the degree to which a river is under-supplied, i.e.  $Q_s \leq Q_c$ . All other model parameters are kept fixed and the tectonic forcing is the same for all the experiments shown here, with the exception of two experiments discussed in 'Structural control of the main drainage divide' and 'Influence of varying  $L_f$ '. By varying  $L_f$ , the average ratio of sediment flux relative to transport capacity will vary (see 'Morphologic significance of  $L_f$ '), but for a non-steady-state system it is difficult to define a simple relationship between  $L_f$  and  $Q_s/Q_c$ . Thus, to aid the interpretation of our modelling results we define instead the maximum amount of sediment,  $(Q_s)_{\max}$ , that will be entrained for a given  $L_f$  and  $Q_c$  by setting  $Q_s = 0$  (zero initial sediment load) in Eqn. (1) and integrating  $dh/dt$  with respect to drainage area,  $A$ . If  $A$  is sufficiently small, such that  $dh/dt$  is constant, then we obtain

$$\frac{(Q_s)_{\max}}{Q_c} = \frac{A}{WL_f}. \quad (6)$$

In our numerical model, if  $A$  is the size of one cell, then  $A = dx^2$  ('The surface process model'). If we assume for simplicity  $W \sim dx$  then, from Eqn. 6,  $(Q_s)_{\max}/Q_c$  can be approximated by the ratio of two length scales within the model, i.e.  $dx/L_f$ .

In this study we consider  $10 \text{ km} < L_f < 100 \text{ km}$ , which corresponds approximately to  $0.01 < (Q_s)_{\max}/Q_c < 0.1$ . Thus most of the results we show are for rivers that remain relatively under-supplied under conditions of increasing  $Q_c$  such as may result from channel steepening due to fault movement. For smaller values of  $L_f$ , i.e. larger  $(Q_s)_{\max}/Q_c$ , we found that the topography generated by faulting is obliterated by fluvial erosion. This is due to the strong diffusive nature of the fluvial incision when  $L_f$  is small (Eqn. (5)). We first present results for a single value of  $L_f$ , and then in 'Influence of varying  $L_f$ ' show how these results may vary.

### Temporal evolution

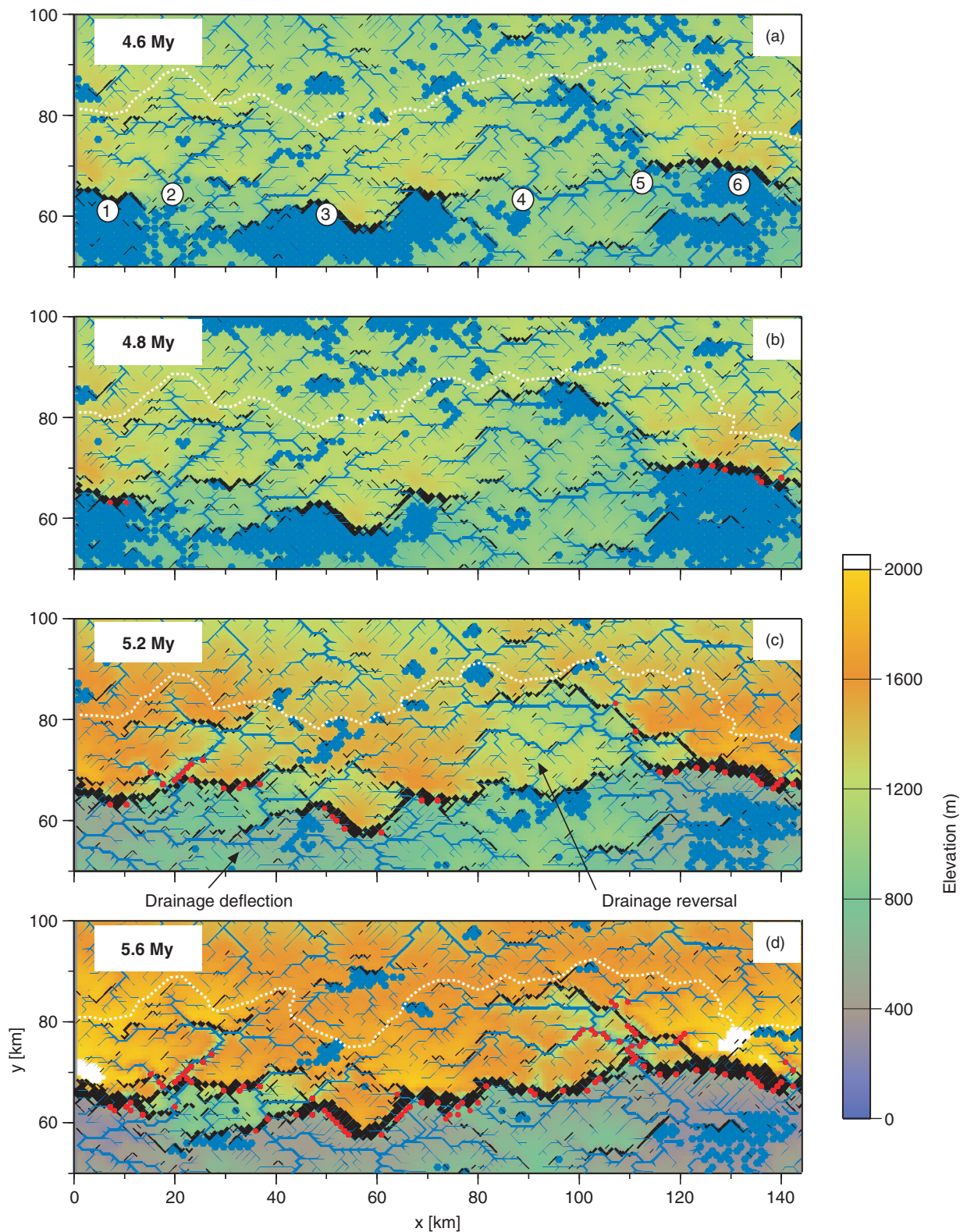
The evolution of the landscape for  $L_f = 45 \text{ km}$  ( $(Q_s)_{\max}/Q_c = 2.5\%$ ) is summarised in Figs 4–7. Note that there is no pre-existing topography or antecedent drainage network imposed; all the surface processes are responding to the topography generated by fault growth as explained in 'The tectonic model'. The purpose of this part of the study is to investigate how the surface processes included in this model respond to the transition from an unlinked diffuse fault array to a single major through-going fault.

Figure 4 shows the topography, cumulative erosion and deposition, and fluvial network that evolve in response to fault growth at four stages in the evolution. Figure 5 summarises the catchment geometry and Fig. 6 summarises the main features of catchment evolution over time. Fault throw at several points along the linking fault array is

shown as a function of time in Fig. 7, along with the temporal occurrence of landslides (Fig. 7a). One of the most important features to note in these figures is the location of the main drainage divide relative to the emerging fault array. For example, by 5.6 Myr (e.g. Fig. 4d and h) the main fault is clearly defined by an irregular scarp that extends right across the model at  $y \approx 65 \text{ km}$ . Although the main drainage divide is also quite irregular along strike, it clearly sits well into the footwall of this fault, i.e.  $\sim 15\text{--}20 \text{ km}$  away from the scarp. This position is established relatively early on in the evolution of fault linkage (i.e. by 3.6 Myr) and changes very little over time (Fig. 4). As a result of the divide location there are several large (i.e.  $\gg 100 \text{ km}^2$ ) catchments that drain across the fault into the hanging wall. There are also numerous much smaller catchments that develop along the front of the fault scarps that are generally very steep and have drainage areas of  $10\text{--}20 \text{ km}^2$ . For purposes of clarity we refer to the former as *hinterland catchments* and the latter as *frontal catchments*, as illustrated in the summary diagram of Fig. 5. Collectively they are referred to as *footwall catchments*. Note that according to this definition the numerical modelling study of Densmore *et al.* (2003), with which we compare some of our results, relates primarily to the evolution of frontal catchments on a length scale of  $< 20 \text{ km}$  (see also Densmore *et al.*, 2004) and does not address hinterland catchment development. The hinterland catchments are typically elongated parallel to fault strike (e.g. Figs 5 and 6), reflecting the strong control that fault growth exerts on the uplift field in the absence of a pre-existing topography.

In spite of the relatively fixed position of the main drainage divide over time, the boundaries of the hinterland catchments fluctuate considerably, particularly before  $\sim 5.0 \text{ Myr}$  (e.g. catchment (v); Fig. 6). This is partly due to the coarse resolution of our model which tends to enhance river capture, but, as we show below, it is also related to the evolution of the fault pattern. In some cases the drainage network is deflected around the ends of growing fault segments and in other cases flow is reversed when a river is defeated by a rapidly growing (and back-tilting) scarp. These processes result in complex changes to the size and shape of catchments through time and the locations of rivers entering the basin, highlighted in Fig. 6. For example, between 4.0 and 4.2 Myr there is a prominent drainage capture event of catchment (v) by catchment (iv) so that catchment (v) shrinks to a fraction of its former size, but by 4.6 Myr catchment (v) has re-established most of its original drainage area. Eventually at 5.0 Myr, the river emerging from catchment (iv) is defeated by the onset of faulting at this location and the drainage is reversed and incorporated into catchment (v) which becomes significantly enlarged (Fig. 6).

A similar competition is observed between catchments (ii) and (iii) although to a lesser extent. Note that the river exiting catchment (ii) continues to incise and drain into the hanging-wall basin even after the onset of faulting at this location at 4.6 Myr (see 'River incision across active fault scraps'). Consequently, even though catchment (iii)



**Fig. 4.** (a–d) Evolution through time of landscape produced by the coupled model at (a) 4.6 Myr, (b) 4.8 Myr, (c) 5.2 Myr and (d) 5.6 Myr. Topographic scale is same as Fig. 1. Fault scarps are show as black areas with line thickness proportional to fault displacement. Blue lines are channels with line thickness proportional to water discharge. Blue dots are lakes. Red dots indicate locations of landslide initiation. White dashed line shows main drainage divide. Numbers 1–6 in (a) indicate the points where fault throw vs. time curves have been extracted and plotted in Fig. 7. Figures (e–f) show cumulative erosion (red) and deposition (green) for same model times. Purple dashed line shows main drainage divide. Circles indicate landslides, as in (a), with relative magnitude indicated by grey shade, from large (black) to small (white). Black lines show locations of main fault segments. Large areas of the footwall have average erosion rates of  $< 20 \text{ mm kyr}^{-1}$  (white areas) even at 5.6 Myr due to fact that the initial topography is flat and topographic steady state is never achieved ('Coupling the tectonic and surface process models').

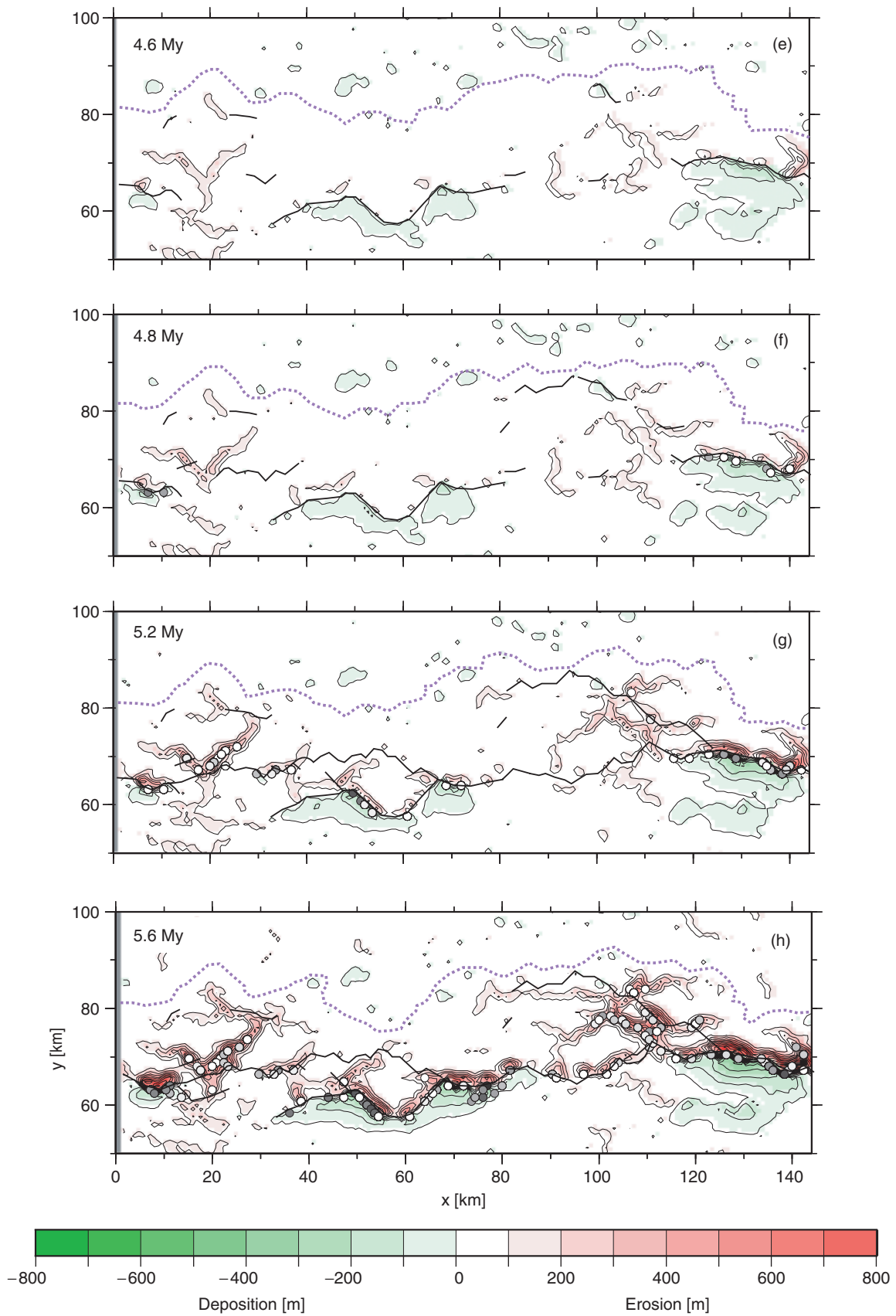


Fig.4. Continued.

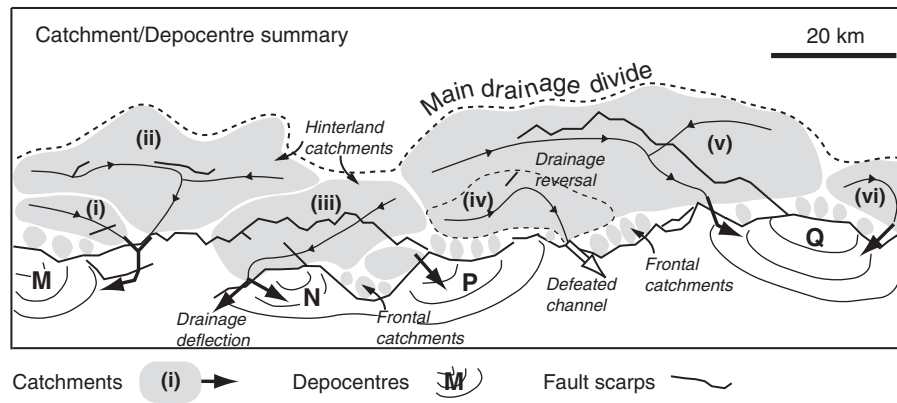


Fig. 5. Diagram summarising overall catchment/depocentre geometry, footwall drainage pattern, position of the linked fault scarp and main drainage divide, derived from panels shown in Fig. 4. Hinterland catchments are labelled from (i) to (vi). Main depocentres are indicated by curved lines in the hanging-wall area and are labelled M, N, P, Q. Large black arrows indicate main sediment entry points and dispersal into hanging-wall basin; large white arrow indicates river outlet that becomes defeated by growing fault.

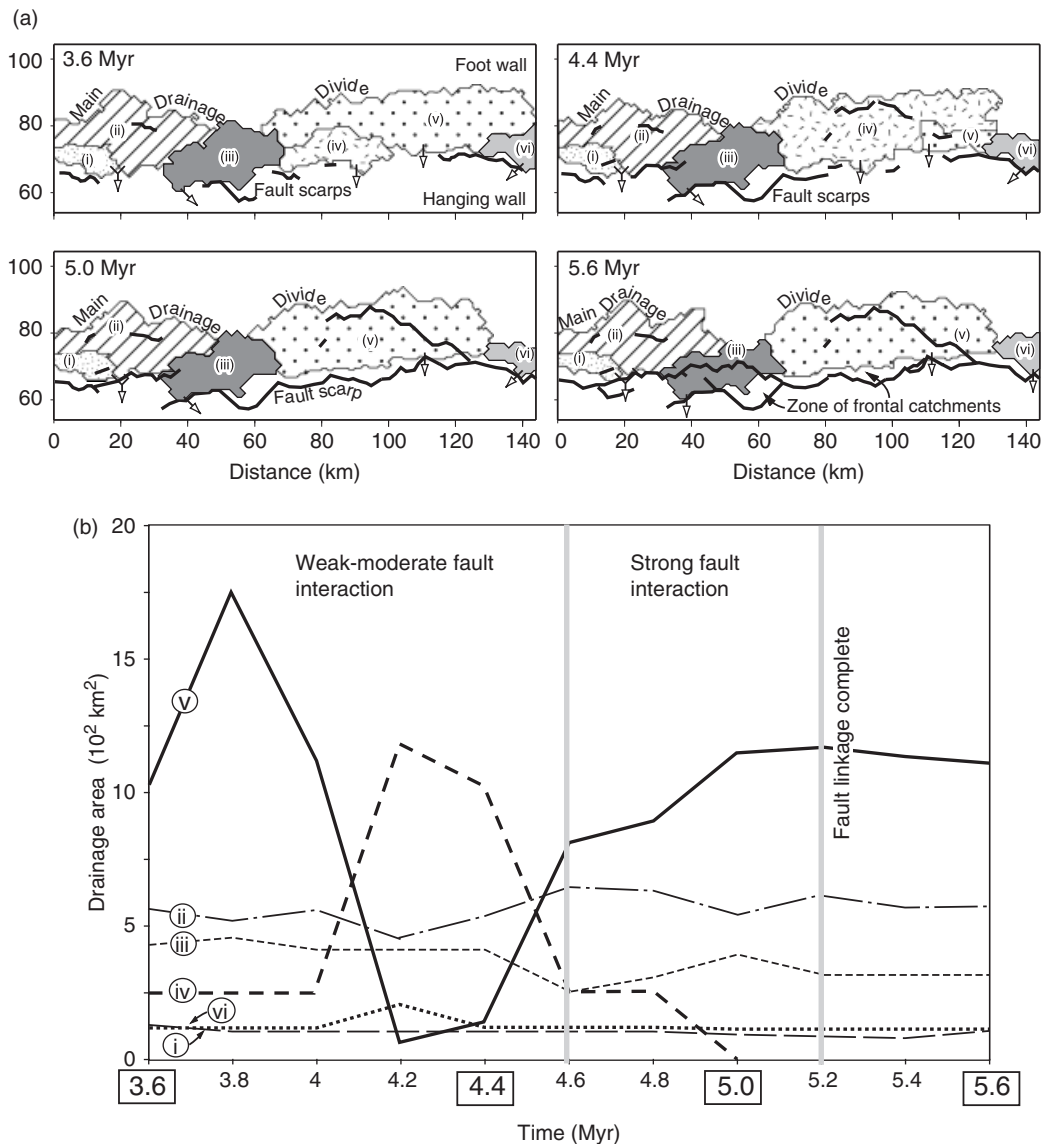


Fig. 6. (a) Maps showing the plan view catchment geometry at 3.6, 4.4, 5.0 and 5.6 Myr; arrows indicate outlets into hanging-wall basins. (b) Variation of drainage area through time for the six largest hinterland catchments (labelled (i)–(vi), as shown in part (a) and Fig. 5).

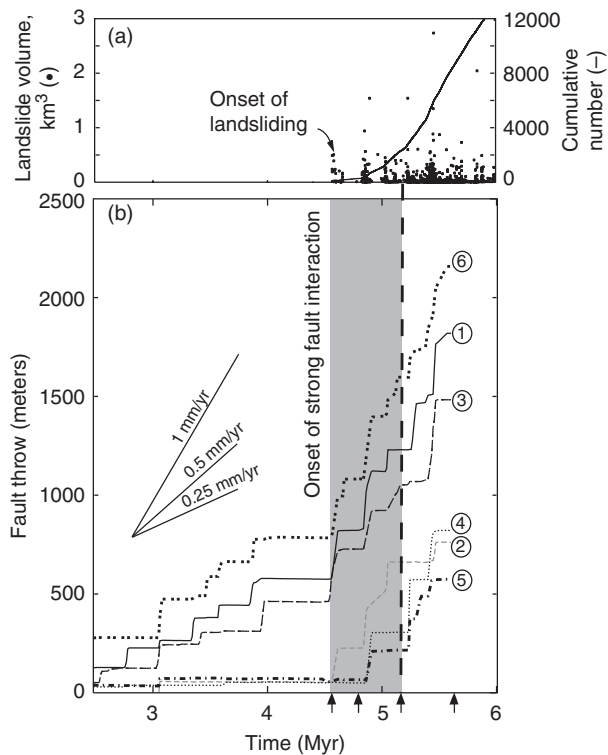


Fig. 7. (a) Landslide volume (in  $\text{km}^3$ ) and cumulative number of landslides, compared with (b) fault throw as a function of time at six different points along the linking fault array. See Fig. 4 for locations of points 1–6. Reference slip rate lines shown for 0.25, 0.5 and  $1 \text{ mm yr}^{-1}$ . Arrows on horizontal axis indicate the time snapshots of the four maps shown in Fig. 4. Vertical grey bar indicates the time interval between the onset of strong fault interaction (4.6 Myr) and fault linkage (5.2 Myr), indicated by vertical dashed line.

drains through a prominent relay zone that is breached relatively late on the fault evolution it is not the largest catchment because much of the footwall in this area is drained through catchment (ii) throughout the entire model run. Thus the size of a footwall catchment is not simply determined by the size of the relay zone through which it drains out into the hanging wall; it is actually controlled by the growth history of adjacent fault segments. Although this result is in broad agreement with the conclusions of Densmore *et al.* (2003), the fault growth history in our model is strongly controlled by elastic interaction between fault segments, a process not modelled by Densmore *et al.* (2003). Elastic interaction results in significant variations in the timing and rate of movement of individual fault segments depending on their location relative to other active structures (Cowie, 1998). Interaction results in instability in the geometry of catchments (ii)–(iv) and (vi) in particular, because these catchments develop and discharge across the fault in areas where the variations in throw and throw rate are greatest, i.e. zones of strongest interaction and incipient linkage before  $\sim 5.2$  Myr. In contrast, the most stable of the hinterland catchments are (i) and (vi) (Fig. 6) because they develop within fairly restricted areas on the growing footwalls of large fault segments that established their length early on in the evolution.

After 5.0 Myr the catchment geometry becomes much more stable (Fig. 6). Although the rivers that drain into the hanging wall from the hinterland catchments initially exploit gaps or displacement lows along the fault array, just as described from field studies (e.g. Eliet & Gawthorpe, 1995), most of these rivers continue to incise across the scarp even after the fault is fully linked so that they then become *locally antecedent*. In other words, they predate the formation of some sections of the final fault geometry, but they are contemporaneous with fault development on a regional scale. As the rivers begin to incise into the growing footwall, river capture events are suppressed even in the upper reaches and it is this that eventually stabilises the catchment boundaries (Fig. 6). We show in ‘Influence of varying  $L_f$ ’ that the degree of river incision depends strongly on the value of  $L_f$  but for this example we see that the upper reaches of the rivers draining the footwall are affected by significant incision by 5.6 Myr (Fig. 4h). The degree to which these rivers can incise is also controlled by the assumption of constant channel width in Eqn. (1) (see ‘Hydraulic geometry – channel width,  $W$ ’). We return to this point in the Discussion.

#### Timing and character of landslide activity

During the first 4.6 Myr of the landscape evolution, landslides do not occur because the low total fault throws and low slip rates during this time period mean that fluvial erosion is able to maintain the surface slopes below the threshold for landsliding (Fig. 7). However, after 4.6 Myr landsliding becomes an important surface process with each pulse of rapid fault slip generating a cluster of landslides (Fig. 7a). The largest landslides, in terms of volume, occur near the centres of the largest, highest slip rate fault segments (Fig. 4e–h). These are the first landslides to be generated and they coincide with the onset of more rapid fault slip associated with fault interaction (at 4.6 Myr; Figs 4 and 7). Along the channels that drain across the fault from the footwall into the hanging wall smaller volume landslides also occur on the valley sides upstream of the fault scarp. These smaller landslides occur mainly after  $\sim 5.0$  Myr and are the result of fluvial incision into the footwall as the elevation and uplift rate of the footwall increase. The morphology of the incised fluvial network and the velocity of propagation both depend on  $L_f$  (see ‘Morphologic significance of  $L_f$ ’ and ‘Influence of varying  $L_f$ ’). In general, fluvial incision causes deepening of the valleys leading to collapse of the valley sides by landsliding. Figure 4e–h shows that fluvial incision propagates upstream from the fault scarp into the footwall over time, generating more small volume landslides. The timing, location and magnitude of landslides are used in the Discussion to infer variations in the nature of sediment input to the hanging-wall depocentres.

#### Structural control of the main drainage divide

One of the most consistent and significant results derived using this model is the location of the main drainage divide

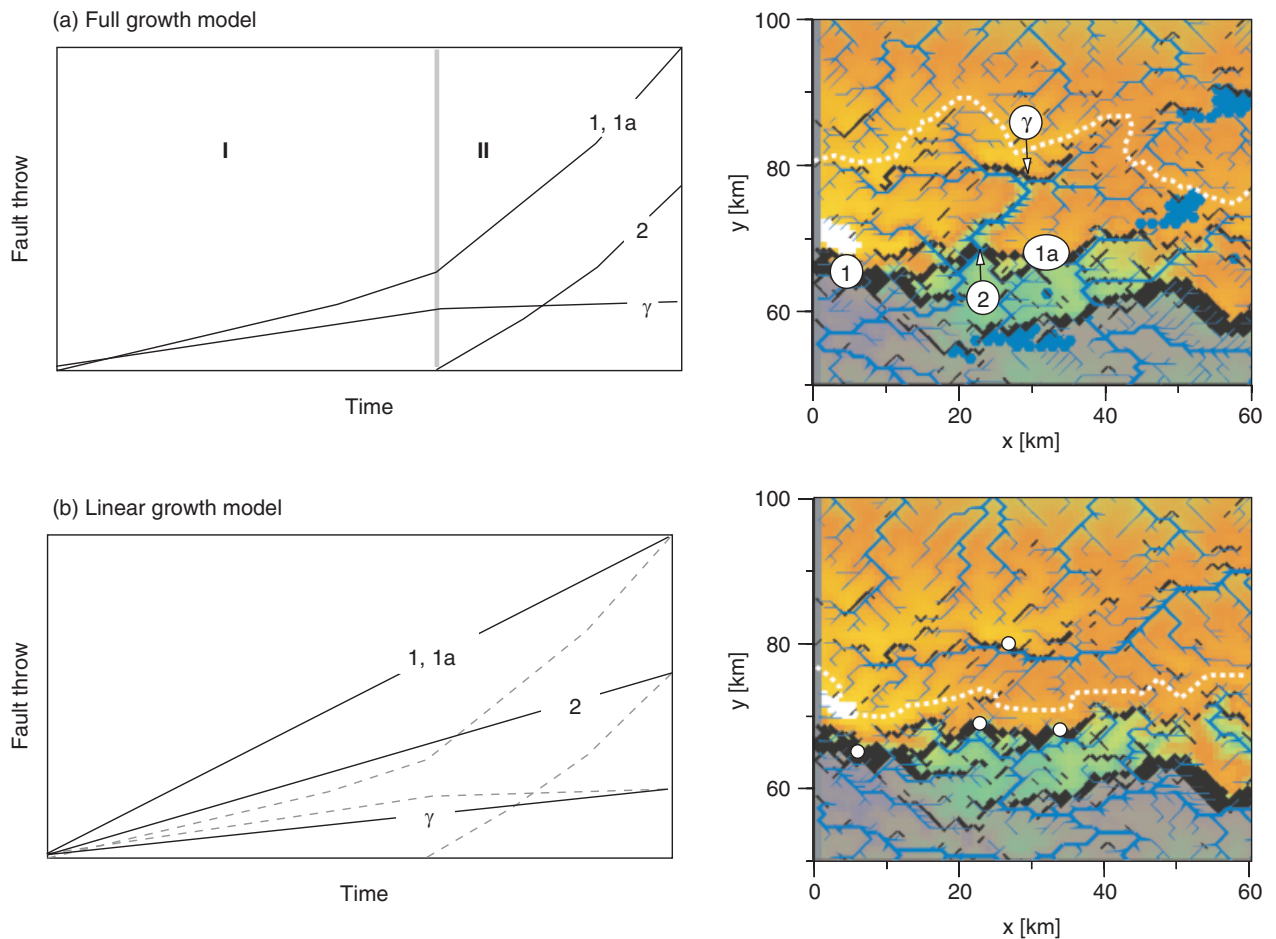


**Fig. 8.** (a) Model landscape after 5.6 Myr for full fault growth model, compared with (b) the landscape at 5.6 Myr obtained for linear fault growth. Colour scheme and locality numbering scheme explained in Figs 1 and 4. Landslides have been removed for clarity. The difference in the tectonic forcing used in the two models is illustrated by the throw vs. time graphs on the left for points 1, 1a, 2,  $\gamma$ , located in (a) and shown by white dots in (b). Locality  $\gamma$  is same as in Fig. 1; locality 1a refers to continuation of scarp where localities 1 and 2 are located in Fig. 4. Time intervals I and II, referred to in (a), are explained in ‘Structural control of the main drainage divide’. Note position of main drainage divide (white dashed line) relative to the main fault scarp differs significantly between the two models.

~15–20 km into the footwall of the major basin-bounding fault (Figs 4–6). This distal position of the main divide cannot be attributed to headward retreat into the footwall of a major fault because the divide is established when the fault is still highly segmented (Figs 4 and 6). The divide location is particularly significant for the volume of sediment supplied to the hanging-wall basin because between the main divide and the scarp there are several very large hinterland catchments (Figs 5 and 6). The timing of formation of these large catchments relative to hanging-wall subsidence has important implications for sediment supply and thus facies development within the growing depocentres.

In order to understand how the history of fault growth is controlling the main drainage divide location we perform an experiment, shown in Fig. 8, between the ‘full’ fault growth model and a ‘linear’ fault growth model. The ‘full’ growth model is the one used in all the other model runs shown in this paper in which all 125 maps of elevation change are used for updating the topography at each time step as explained in ‘The tectonic model’. The ‘linear’ model uses just the final topography and linearly inter-

polates at each time step between the origin, where the elevation is zero everywhere, and the final elevation of each node. Thus nodes with low final elevations have constant low slip rates, whereas nodes with high final elevations have constant high slip rates as illustrated in Fig. 8b. Therefore there are no effects due to elastic interaction between fault segments in the ‘linear’ growth model. By conducting this simple experiment we are able to demonstrate explicitly the impact of fault interaction on the development of the footwall drainage network.

The drainage pattern resulting from the ‘linear’ fault growth model is quite different in a number of important ways from that obtained using the ‘full’ fault growth history (Fig. 8). The main drainage divide is located only a few kilometres behind the scarp when fault interaction effects are suppressed (Fig. 8b). This relatively short distance reflects the magnitude of drainage divide migration that might occur by headward erosion in our model. Headward erosion by itself is clearly not able to generate the formation of large hinterland catchments in the footwall of the fault.

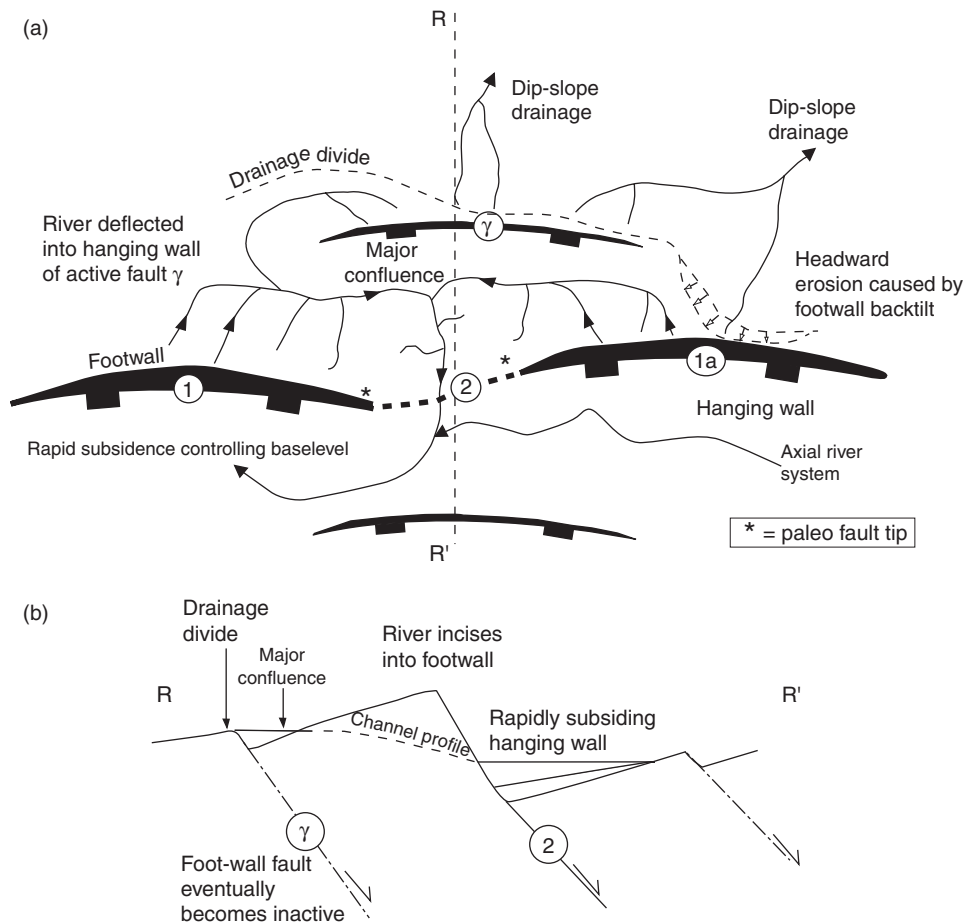


Fig. 9. Schematic diagram summarising key features of the full fault growth model shown in Fig. 8a to explain how fault interaction leads to the development of the trellis drainage networks in the coupled model. (a) Plan view with localities 1, 1a, 2,  $\gamma$  from Fig. 8a marked. (b) Cross-section from  $R$  to  $R'$  to show how drainage pattern relates to footwall uplift at locality 2 after fault linkage.

From this experiment it becomes clear that the most important thing controlling the distal location of the main drainage divide is the large variation in fault growth rates that precedes the phase of fault segment linkage at  $\sim 5.0$  Myr (phase I, Fig. 8a). During this early phase of the 'full' growth model, many faults are active (Fig. 2) including faults that ultimately die out and become incorporated into the footwall block of larger structures (e.g. locality  $\gamma$ ; Figs 1, 2 and 8a). Rivers draining down the dip slopes of large early-formed segments (e.g. localities 1 and 1a; Fig. 8a) are deflected into a fault parallel direction by subsidence within the hanging wall of these other active structures (locality  $\gamma$ ; Figs 1, 8a and 9). However, because the fault growth rates at localities 1 and 1a are higher than at locality  $\gamma$ , these same rivers ultimately turn and flow into the more rapidly subsiding depocentres in the hangingwall to points 1 and 1a (Fig. 9). This is possible because the uplift rate at locality 2 is extremely low during phase I. The river that enters the basin at locality 2 has established a significant upstream drainage area by the time the slip rate at 2 increases during phase II. In plan view the drainage network geometry contains characteristically hook-shaped rivers that drain away from the basin in their upstream reaches but ultimately turn and flow into the

basin in their lower reaches (Fig. 9). Such patterns are a common feature of extensional settings and are usually referred to as 'trellis' drainage networks, as we discuss below. Note that in the 'full'-growth model there are two pathways for the same footwall uplift to supply sediment to the adjacent depocentre: one is via short, steep frontal catchments, whereas the other is via very much longer, generally lower gradient, routes through hinterland catchments.

In contrast, in the 'linear' fault growth model, the fault labelled  $\gamma$  is always active but at a very low rate of slip (Fig. 8b) and it exerts very little influence on the early development of the drainage network. Moreover, locality 2 continuously accumulates fault throw at a fairly high rate so that there is no longer a pathway for the river to enter the basin. As a result most of the footwall area is drained by an extensive channel network that flows down the dip-slope away from the hanging-wall basin (Fig. 8b). Because of the proximal position of the main drainage divide relative to the scarp, the dominant route for sediment to enter the adjacent depocentre is via short, steep frontal catchments and the potential sediment source areas are much more limited.

Although the distal position of the main drainage divide in the 'full' growth model is established relatively early on

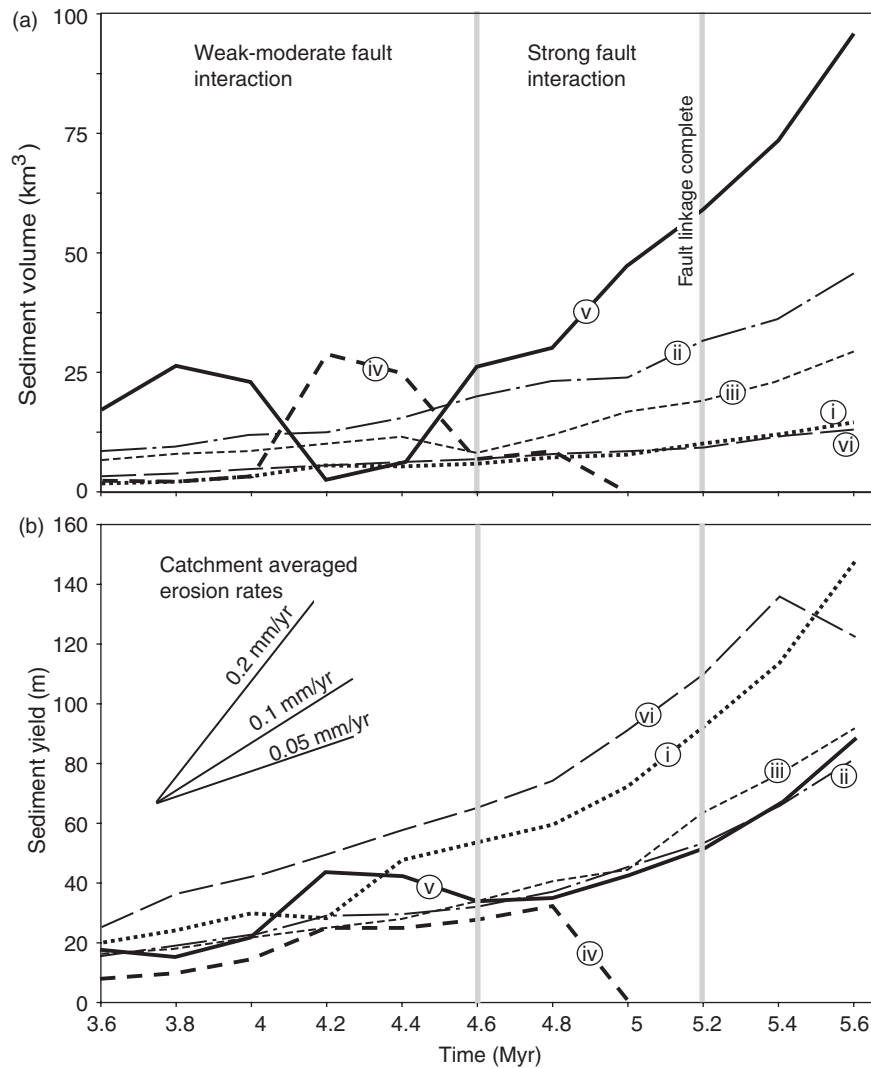


Fig. 10. (a) Sediment volume compared with (b) sediment yield (sediment volume/drainage area) through time for the six largest catchments within the footwall (see Figs 5 and 6 for catchment numbers). Slope of yield vs. time curve gives catchment-averaged erosion rate; reference erosion rate lines shown for 0.05, 0.1 and 0.2 mm yr<sup>-1</sup>.

during fault development, it is also controlled by the competition between headward erosion within the footwall catchments that drain across the fault into the hanging wall (both frontal and hinterland catchments) and headward erosion within the catchments that continue to drain down the dip-slope of the uplifting footwall. Headward erosion within the frontal and hinterland catchments depends on base-level fall along the fault, whereas the dip-slope drainages erode headward because they become steeper as the footwall area is back-tilted. If the two rates are approximately in balance the main drainage divide location is relatively stable through time as generally shown by Figs 4 and 6a. Interestingly, where back-tilting of the footwall is sufficiently rapid, as it is near the centres of long rapidly growing fault segments (e.g. locality 6; Figs 4 and 7b), the main drainage divide can actually migrate locally by several kilometres *towards* the fault scarp by capturing the headwaters of hinterland catchments (Fig. 6a at 5.6 Myr). This direction of drainage divide migration is en-

tirely contrary to what one would intuit from a model in which fault growth by segment interaction and linkage is ignored (see also 'Influence of varying  $L_f$ ').

### Sediment supply variations from footwall catchments in space and time

In addition to analysing catchment size and geometry we also calculate the total cumulative sediment volume (in m<sup>3</sup>) emerging into the hanging-wall basin through time from the hinterland catchments (Fig. 10). We focus on the time interval between 3.6 and 5.6 Myr, which encompasses the time of fault linkage and acceleration in slip rate (Fig. 7). In order to be able to compare in a meaningful way the sediment volumes derived from the different catchments through time we also calculate sediment yield, which is total sediment volume divided by drainage area. Sediment yield is thus a measure of the average amount of erosion across each catchment (in m); high sediment

volume does not necessarily mean high sediment yield and vice versa. The slope of the sediment yield vs. time curves gives catchment averaged erosion rate.

Most of the catchments show an overall increase in both yield and volume through time with the exception of catchment (iv), which is defeated by a growing fault scarp at  $\sim 5.0$  Myr (Figs 4–6). There are local variations superimposed on this overall increase that can be related to the changes in catchment geometry (Fig. 6). Figure 10a also shows that the volume of sediment supplied by each catchment is a function of its size, so that larger catchments supply more sediment (e.g. Whipple & Trayler, 1996). With respect to sediment yield, however, the converse is true (Fig. 10b). Catchments (i) and (vi)

produce the lowest sediment volumes but the highest yields whereas catchments (ii), (iii), (v) have lower yields that are very similar in magnitude despite significant differences in their drainage areas (Fig. 6). The high yields of catchments (i) and (vi) are due to the fact that they are located in the immediate footwall near the centres of large fault segments where the throw and throw rates are high (curves 1 and 6 in Fig. 7b). As a consequence, catchments (i) and (vi) also experience the highest erosion rates and are deeply incised (Figs 4e–h and 10b). These results are consistent with the conclusions of Densmore *et al.* (1998, 2003), in that the position of a catchment relative to maximum fault uplift rates determines sediment yield and erosion rates.

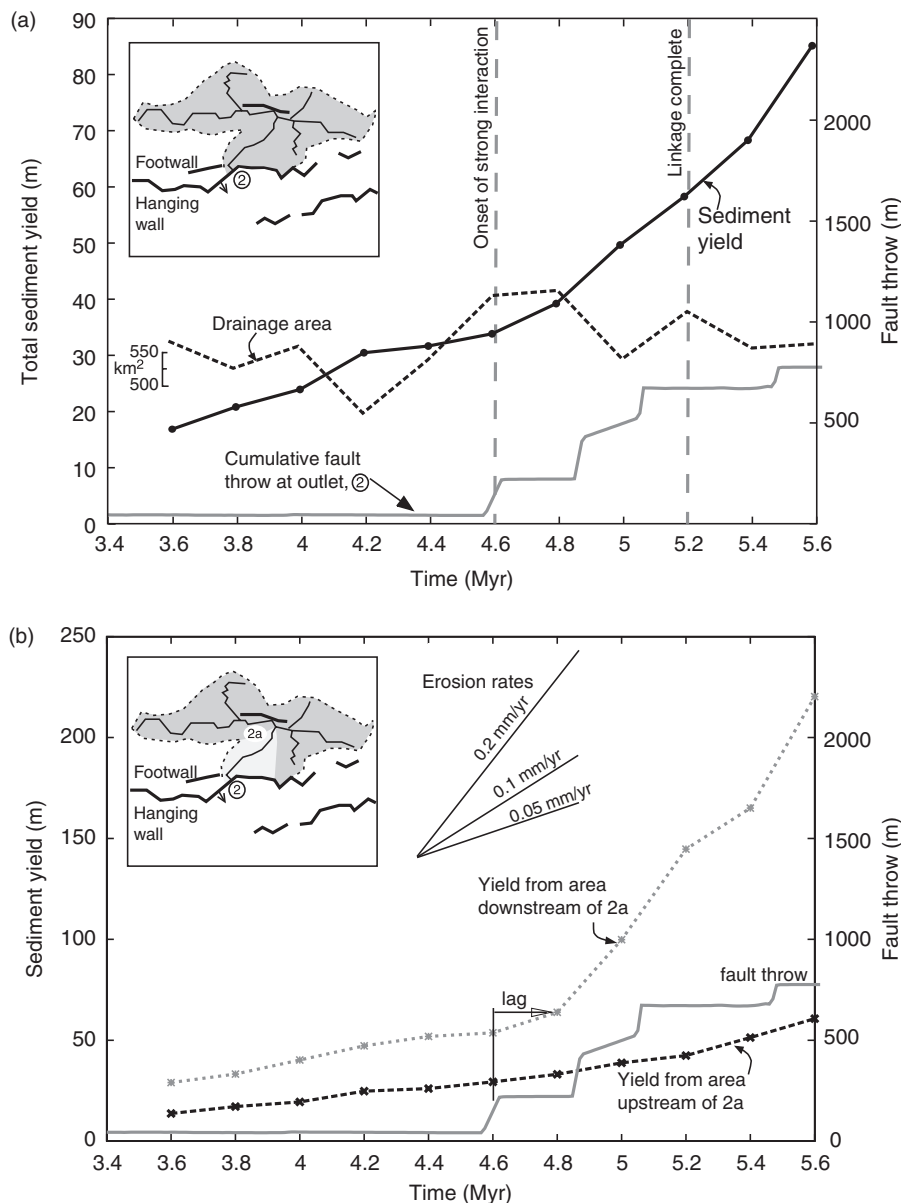


Fig. 11. (a) Sediment yield (solid black line), drainage area (dashed line) and fault throw (grey line) through time for catchment (ii) in Fig. 5, inset shows simplified catchment and fault geometry and outlet at locality 2 (see Fig. 4a). (b) Detailed view of sediment yield through time for two different parts of the catchment shown in (a). Slope of yield vs. time gives catchment-averaged erosion rate; reference erosion rate lines shown for 0.05, 0.1 and 0.2 mm yr<sup>-1</sup>. Inset shows how catchment is sub-divided into drainage area upstream of the main confluence at 2a, and drainage area between 2a and 2.

The similarity in sediment yield from catchments (ii), (iii) and (v), in spite of their widely differing and temporally changing drainage areas, is also reflecting proximity to areas of significant or rapid footwall uplift. For example, catchment (iii) has a smaller drainage area than (ii) and (v) but headwater channels in this catchment are located in an area of substantial and rapid footwall uplift of early-formed fault segments bounding depocentres N and P (curve 3 in Fig. 7b). In contrast footwall topography and uplift rates are low in the areas of catchments (ii) and (v) until at least  $\sim 5.0$  Myr. What is clearly illustrated by this analysis is that it is not simply the location of the sediment entry point from a footwall catchment into a basin that is important; it is the spatial extent and location of the headwaters relative to growing footwall highs that ultimately determine both the sediment volume and the yield.

Figure 6 also illustrates the important effect of the fault scarps in deflecting the channel network and thus controlling the sediment input into individual depocentres. For example, the large depocentre that develops in the hanging wall of the central fault segment consists of two sub-basins (N and P). Except for a small steep frontal catchment that feeds directly in sub-basin P, most of the footwall drainage is deflected around the fault tips into the flanking depressions controlled by adjacent faults (sub-basins M and Q). Sub-basin N is occasionally fed by the river emerging from catchment (iii), but at other times this drainage is deflected into sub-basin M. Significant erosion of the fault scarp bounding sub-basins N and P occurs by landsliding in addition to fluvial erosion within small ( $10\text{--}20\text{ km}^2$ ) steep frontal catchments. Thus the sediments that accumulate within this depocentre will be quite distinct from those of neighbouring sub-basins (M and Q) which are fed by the largest footwall catchments: (ii) and (v).

#### *Sediment yield variations through time for a single footwall catchment*

Rather than restricting our analysis to the overall sediment volume produced by all footwall catchments we are able to investigate spatial and temporal variations in sediment supplied by individual catchments. We showed in Fig. 10 that the hinterland footwall catchments can represent a significant contribution to total sediment volume supplied to the hanging-wall basin, so it is particularly important to understand how sediment supply from such a catchment varies as the fault array evolves through time. Thus in Fig. 11 the sediment yield through time for catchment (ii) is compared with the accumulation of throw on the fault where the river exits the footwall (locality 2 in Figs 4, 7b, 8 and 9). Also shown for comparison is the drainage area for the same catchment. The sediment yield clearly increases as fault throw increases. What is interesting is that the increase in sediment yield begins before 4.6 Myr, which is the time at which faulting at locality 2 initiates (Fig. 11a). The increase in yield is not due to variations in drainage area

(Fig. 11a); fluctuations in drainage area of the order of 10–20% do occur through time (see also Fig. 6) but generally affect only the upper parts of the catchment and result in minor variations in sediment yield. Obviously, sediment is derived from the entire catchment and thus the variation in yield must reflect the average uplift and erosion across the whole catchment area, not just the onset of faulting at 2.

In order to understand how the variation in sediment yield is being controlled by the faulting, Fig. 11b shows sediment yield calculated for two distinct parts of the catchment (see locations 2a and 2 in inset to Fig. 11b). The shaded areas in the inset figure show the relative drainage areas of the two parts of the catchment, which are used to calculate the sediment yields for each area. Note that most of the drainage area is upstream of locality 2a where there is a network of channels that drain approximately parallel to the fault scarp and collect water and sediment derived from neighbouring fault segments as well as off the dip slope of the growing footwall (see Fig. 9). Downstream of locality 2a the river drains approximately perpendicular to the fault scarp and is directly incising across the uplifting footwall. The sediment yield from the part of the catchment immediately upstream of the fault (between 2a and 2) does show a clear response to accelerated fault motion at locality 2, with a time lag  $\leq 0.2$  Myr (Fig. 11(b)). In contrast, the upper part of the catchment (upstream of 2a) shows a more gradual increase over time with no obvious change reflecting throw accumulation at 2. This is because the upper reaches are only affected by uplift of adjacent footwall areas before the onset of uplift at 2, as recorded by curves 1 and 3 in Fig. 7b. Figure 11b also shows that erosion rate (the slope of the yield vs. time plot) also differs between these two parts of the catchment after 4.6 Myr, with much higher average rates of erosion ( $0.1\text{--}0.2\text{ mm yr}^{-1}$ ) in the area between 2 and 2a compared with the area upstream of locality 2a ( $< 0.05\text{ mm yr}^{-1}$ ). This is not a static pattern, however, as Fig. 4e–h shows: the wave of incision propagates upstream from the fault scarp into the footwall over time, resetting both channel and hill-slope gradients ('Timing and character of landslide activity' and 'River incision across active fault scarps').

This analysis clearly demonstrates the fact that the three-dimensional nature of the uplift field must be considered to predict the sediment volume entering the hanging-wall basin at a particular point. The large variation in sediment yield (and erosion rate) within the same catchment (Fig. 11b) has implications for the timing of sediment input to a hanging-wall depocentre as well as the sediment calibre that might be derived from a catchment of this type in real rifts ('Nature of sediment supply variations associated with fault interaction and linkage: implications for syn-rift stratigraphic patterns'). The data shown in Fig. 11 convey the temporal variations in sediment yield but they do not allow the relative volumetric contributions from the two parts of the catchment to be compared easily. Thus in Fig. 12 we show, for each time step of the model, cumulative sediment volume produced as a function of distance upstream from the fault, both quantities normalised to

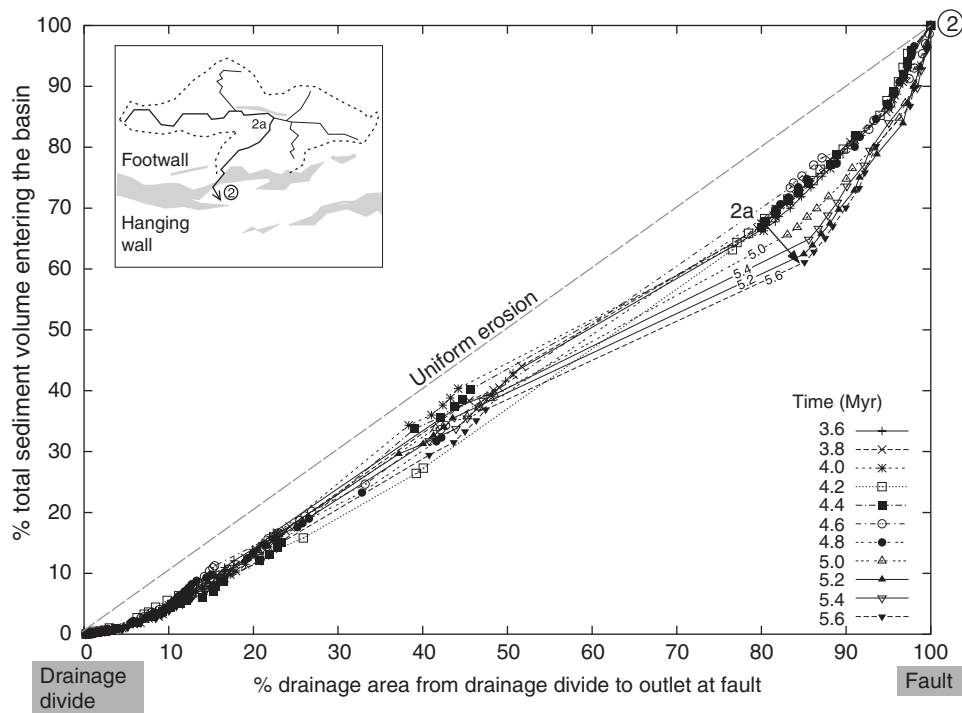


Fig. 12. Normalised sediment volume vs. drainage area for the catchment analysed in Fig. 11. Locality 2 is at the outlet and locality 2a is same as in Fig. 11 and is indicated in inset map. Fault throw variations indicated by width of grey areas in inset map. See 'Sediment yield variations through time for a single footwall catchment' for discussion. Note that the model curves always lie slightly below the uniform erosion line (dashed line) even before 5.0 Myr. This is mainly due to the fact that the initial topography is flat and topographic steady state is never achieved.

permit comparison. The area upstream of locality 2a clearly represents most of the drainage area ( $\sim 80\%$ ) and contributes most ( $\sim 60\text{--}70\%$ ) of the sediment that enters the basin at locality 2 during the entire time interval between 3.6 and 5.6 Myr (Fig. 12). Therefore the increase in sediment yield through time seen in Fig. 11a before 4.6 Myr must be derived from this upstream area and the increase begins even when channel gradients are quite low (see also Fig. 13b). It is the uplift and tilting of the flanking footwall highs that causes this increase and reflects the onset of faulting regionally rather than the local development of the fault scarp at locality 2. In contrast, the catchment downstream of locality 2a represents only  $\sim 20\%$  of the total drainage area ( $\sim 100\text{ km}^2$ ) and contributes  $\sim 30\%$  of the total sediment volume until 4.8 Myr (Fig. 12). However, after 4.8 Myr, the same section contributes at least 40% of the total sediment volume from this catchment (Fig. 12). This is the reach where the channel gradient steepens significantly at  $\sim 5.0$  Myr (Fig. 13b) and where small volume landslides occur on the valley sides (Fig. 4).

In summary, the overall increase in sediment yield from the footwall in response to fault growth, shown in Fig. 11a, is actually made up of two quite distinct components. One component is the significant (in terms of volume) upstream contribution (i.e. upstream of locality 2a), which shows a long-term gradual increase in volume produced by relatively low erosion rates that increase slowly. Superimposed on this gradual increase is the relatively abrupt ( $\leq 0.2$  Myr) appearance of material that is produced by much higher rates of erosion within the proximal footwall

area (between 2 and 2a). Thus sediment yield and erosion rates vary spatially and temporally across a hinterland footwall catchment during a fault linkage event with important consequences for sediment input into the basin.

### River incision across active fault scarps

In this section we investigate the factors controlling the incision rate of the rivers draining the hinterland catchments and thus address the fundamental question of why some rivers are able to maintain their course across a growing footwall uplift whereas others are reversed or deflected around the fault tip. It is commonly assumed that drainage area (as a proxy for river discharge) is the main control, even though discharge is only one of several factors that control river incision rate. What we need to consider is the *change* in stream power along the river channel as it drains across the back-tilting fault block. To maintain its course, a river draining up structural dip until it emerges onto the hanging wall needs to increase its stream power in the face of a tectonic tilt that tends to reduce its gradient downstream. For this model we demonstrate how the downstream increase is achieved in order to develop a greater general understanding of this process, independent of the specific fluvial incision model used here (see also the Discussion).

The drainage patterns developed within the hinterland catchments in our model do not show the usual Hack's Law relationship between drainage area and downstream distance due to the strong tectonic control of catchment

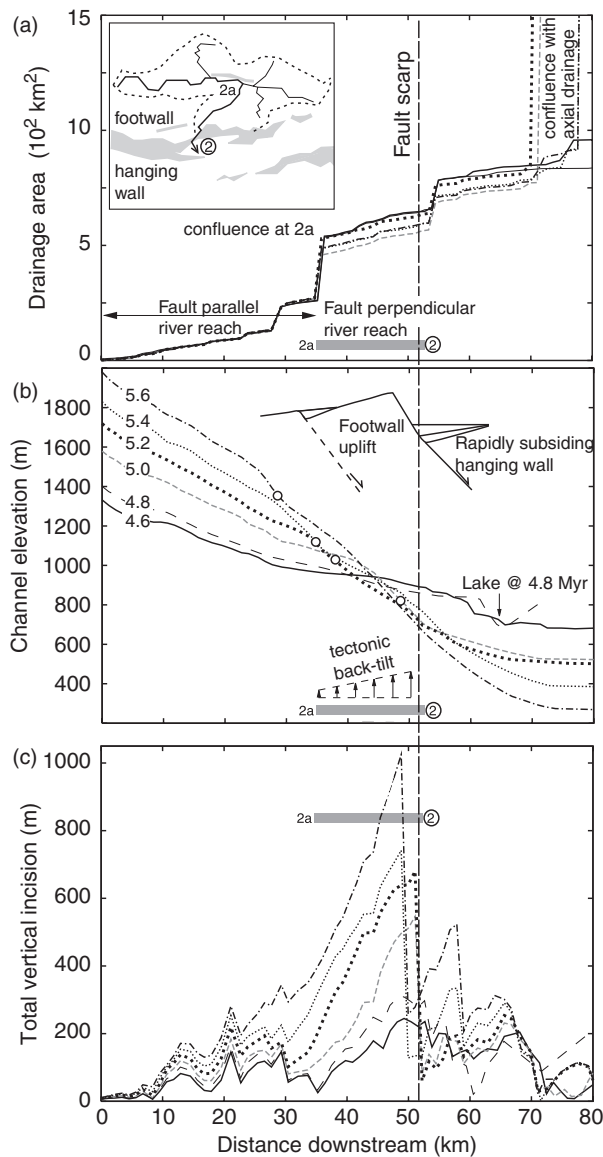


**Fig. 13.** Characteristics of river draining through scarp at locality 2 (see inset map and Figs 4, 11 and 12 for location). Temporal evolution of (a) drainage area, (b) elevation, (c) total vertical incision, vs. downstream distance. Inset map in (a) shows fault geometry with fault throw variations indicated by width of grey areas and main channel indicated by thick black line. Times shown in (b) are in Myr and the same key is used for parts (a) and (c). Total vertical incision is calculated at each time by subtracting the elevation of the channel from the elevation of the uneroded (i.e. tectonic) topography. Circles in (b) correspond to those shown in Fig. 17 and indicate the position downstream of which the channel elevation is in dynamic steady state.

development (Fig. 9). For the river that drains across the fault scarp at locality 2 (Figs 4 and 7b), Fig. 13a shows that most of the discharge of the river is established by the confluence of fault-parallel channels focused by growing footwall uplifts. Where the river turns and drains approximately perpendicular to the fault and incises into the rising footwall the discharge increases only very slowly downstream (between 2 and 2a; Fig. 13a). In spite of this, the total amount of vertical incision increases significantly

downstream along the same reach after 4.6 Myr, which is when faulting at locality 2 initiates (Fig. 13c). The amount of total vertical incision generally also increases through time, whereas river discharge if anything slightly decreases after 4.6 Myr due to river capture (Figs 6 and 13a). As a result of incision the channel gradient upstream of the fault either remains uniform or increases, so that the long profile develops a very low concavity or becomes convex (Fig. 13b). Thus, even though the channel is being actively back-tilted after 4.6 Myr, the slope of the channel increases in the direction of the hanging wall.

Thus it is clear that discharge is not the only control on the ability of the river to maintain its course in this case. One mechanism for increasing the erosive power of a river is to decrease the channel width,  $W$  (Eqn. (1)) (e.g. Fig. 3; Whittaker *et al.*, in press). In our model  $W$  is constant and thus the vertical incision of the channel upstream of the fault is largely driven by changes in channel slope caused by baselevel lowering at the fault scarp. Each time the fault at locality 2 moves, it generates a steep topographic basinward slope right at the scarp that results in an abrupt increase in  $Q_c$ . Footwall incision is then driven by the disequilibrium between  $Q_c$  and the sediment volume  $Q_s$ , as explained in 'The surface process model'. The incision response to a change in  $(Q_c - Q_s)$  at the fault depends on the value of  $L_f$  (Eqn. (1)).

#### *Influence of varying $L_f$*

In 'Morphologic significance of  $L_f$ ' we showed theoretically that the value of  $L_f$  determines how a river will incise in response to a sudden base-level fall. When  $L_f$  is large ( $q_c \gg D_c$ ; resistant lithology), a river in our model mimics the behaviour of a DL system, characterised by the upstream migration of an abrupt knickpoint which migrates at velocity  $\propto 1/L_f$ . When  $L_f$  is small ( $q_c \ll D_c$ ; erodible lithology) the model mimics the behaviour of a TL system which is characterised by a diffusive response. This difference in behaviour is critically important in determining whether a river draining a hinterland catchment in this model will maintain its course or become dammed and/or deflected as fault segment linkage occurs. In this study we have varied  $L_f$  to simulate the full range of behaviour between the DL and TL end-member models.

Figure 14a shows how the long profile of the river draining across the actively growing fault at locality 2 varies as a function of  $L_f$  at 5.2 Myr. When  $L_f = 10 \text{ km}$  ( $(Q_s)_{\text{max}}/Q_c \sim 10\%$ ) the river profile is approximately linear upstream of the fault, but for larger values of  $L_f$  the profile shows a distinct convex reach immediately upstream of the fault and a very low channel gradient upstream of the convex zone. Note that the base of the convex reach remains pinned at the fault and the episodic movement of the fault is a persistent source of disequilibrium between  $Q_c$  and  $Q_s$  (Fig. 7). When the episodic nature of the fault motion is suppressed (Fig. 14b), the over-steepened reach is less pronounced because the river is able to respond more easily to continuous fault motion (i.e. a creeping

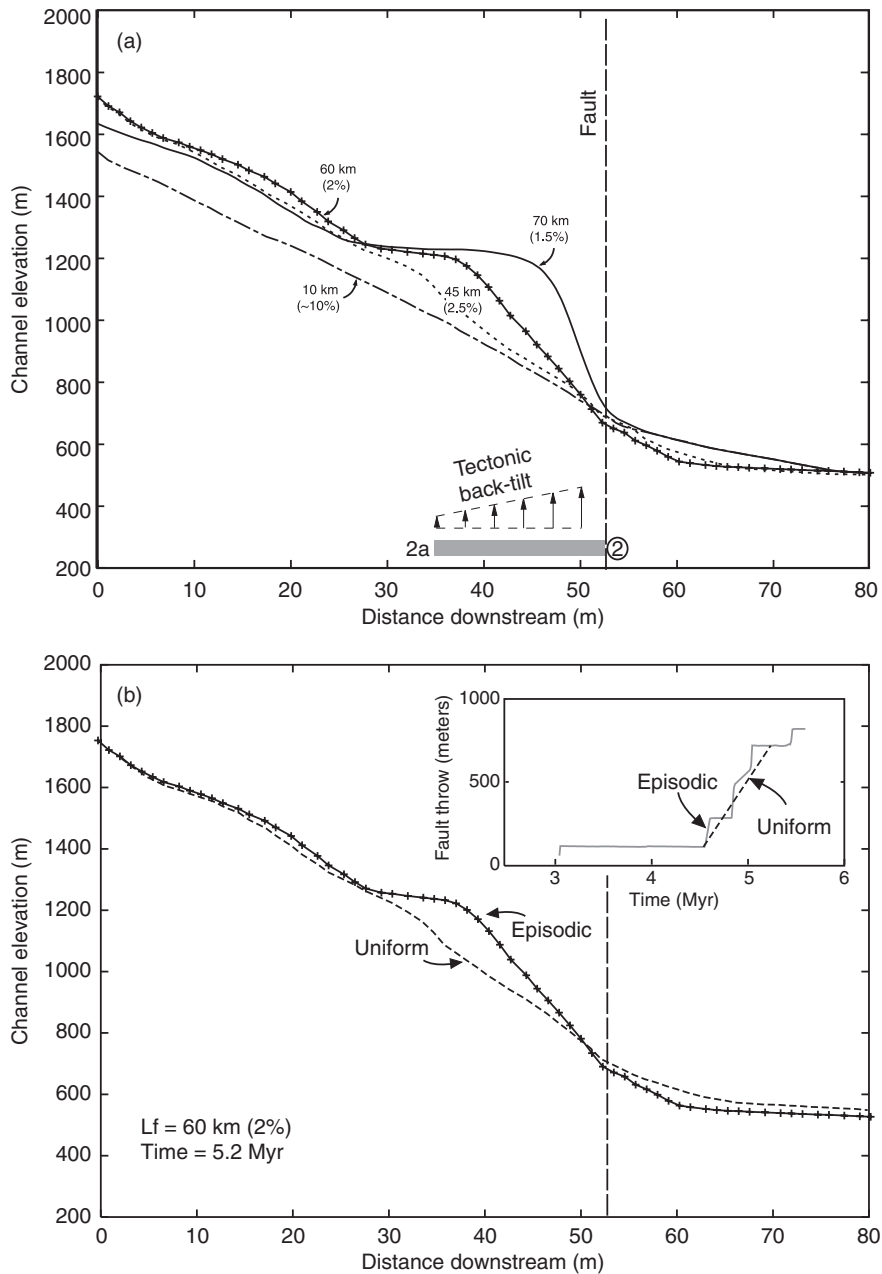


**Fig. 14.** (a) Comparison of long profiles at 5.2 Myr of river draining through scarp at locality 2 (see Figs 4, 11–13 for location of river and point 2) for different values of  $L_f$ . Corresponding ratio  $(Q_s)_{\max}/Q_c$  is shown in brackets. (b) River profile for  $L_f = 60$  km at 5.2 Myr, as shown in (a), compared with the profile obtained for this value of  $L_f$  when fault throw rate at point 2 is uniform between 4.6 and 5.2 Myr, as opposed to episodic (inset graph in (b) shows the two throw–time curves). See ‘Influence of varying  $L_f$ ’ and ‘Deviation from topographic steady state in actively incising channels’ for discussion.

fault), than it can to periods of rapid fault slip interspersed with periods of zero fault slip (i.e. a seismogenic fault). We return to this point in ‘Deviation from topographic steady state in actively incising channels’.

The plan view distribution of footwall erosion also shows a strong dependence on  $L_f$  (Fig. 15). Figure 15(a) shows that, by 5.6 Myr, fluvial incision extends further into the footwall when  $L_f$  is comparatively small with a large number of wide valleys that are well-developed as far as the drainage divide. In contrast, when  $L_f$  is increased to 100 km ( $(Q_s)_{\max}/Q_c = 1\%$ ) (Fig. 15c) erosion remains mainly concentrated along the fault scarp at 5.6 Myr with a small

number of narrow fluvial valleys that incise deeply into the footwall for a short distance upstream of the scarp. The range of morphology seen in Fig. 15 reflects both the influence of  $L_f$  on valley form through the intrinsic concavity (Eqn. (3)) and the fact that the velocity of the incision wave scales as  $1/L_f$  when  $L_f$  is large (Eqn. (4)).

It is evident in Fig. 15 that  $L_f$  also influences the overall position of the main drainage divide along strike. This influence is superimposed on the underlying structural control of the main drainage divide that we showed above. The main divide is maintained by the competition between headward erosion of the dip-slope drainage network and

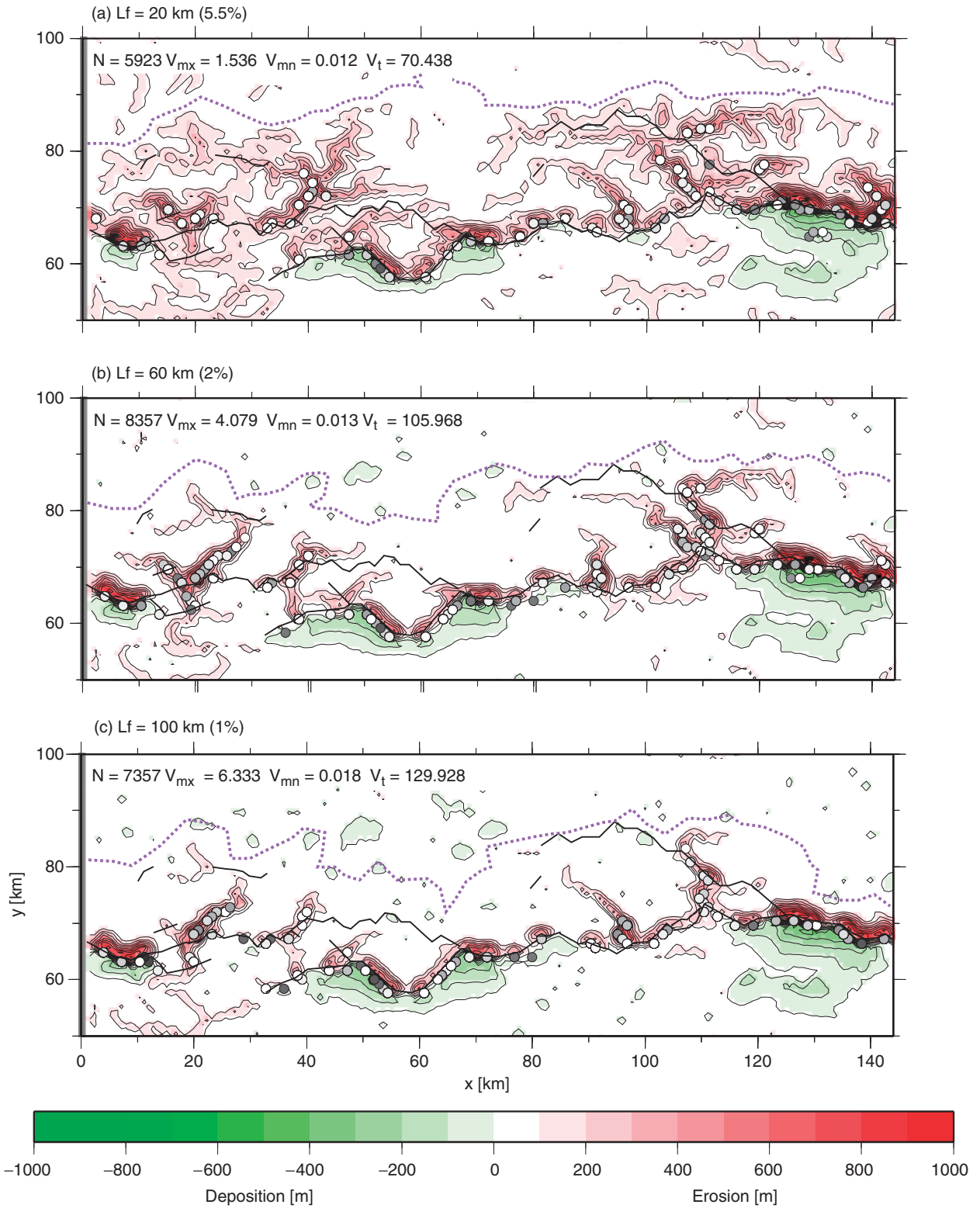


**Fig. 15.** Cumulative erosion (red) and deposition (green) for three different values of  $L_f$  at 5.6 Myr: (a)  $L_f = 20$  km, (b)  $L_f = 60$  km, (c)  $L_f = 100$  km. Corresponding ratio  $(Q_s)_{max}/Q_c$  is shown in brackets. Note that in (c) the drainage divide (purple dashed line) is much more irregular and in places located very close to the fault scarp (black line) for large  $L_f$  ( $(Q_s)_{max}/Q_c$  small). Landslide initiation points are indicated by circles with grey shade representing magnitude from large (black) to small (white).  $N$  = total number of landslides;  $V_{mx}$  = maximum size of landslide (in  $\text{km}^3$ );  $V_{mn}$  = mean size of landslide (in  $\text{km}^3$ );  $V_t$  = total volume of material moved by landsliding (in  $\text{km}^3$ ). Landslides are more numerous and larger when  $L_f$  increases ( $(Q_s)_{max}/Q_c$  decreases). See ‘Influence of varying  $L_f$ ’ for discussion.

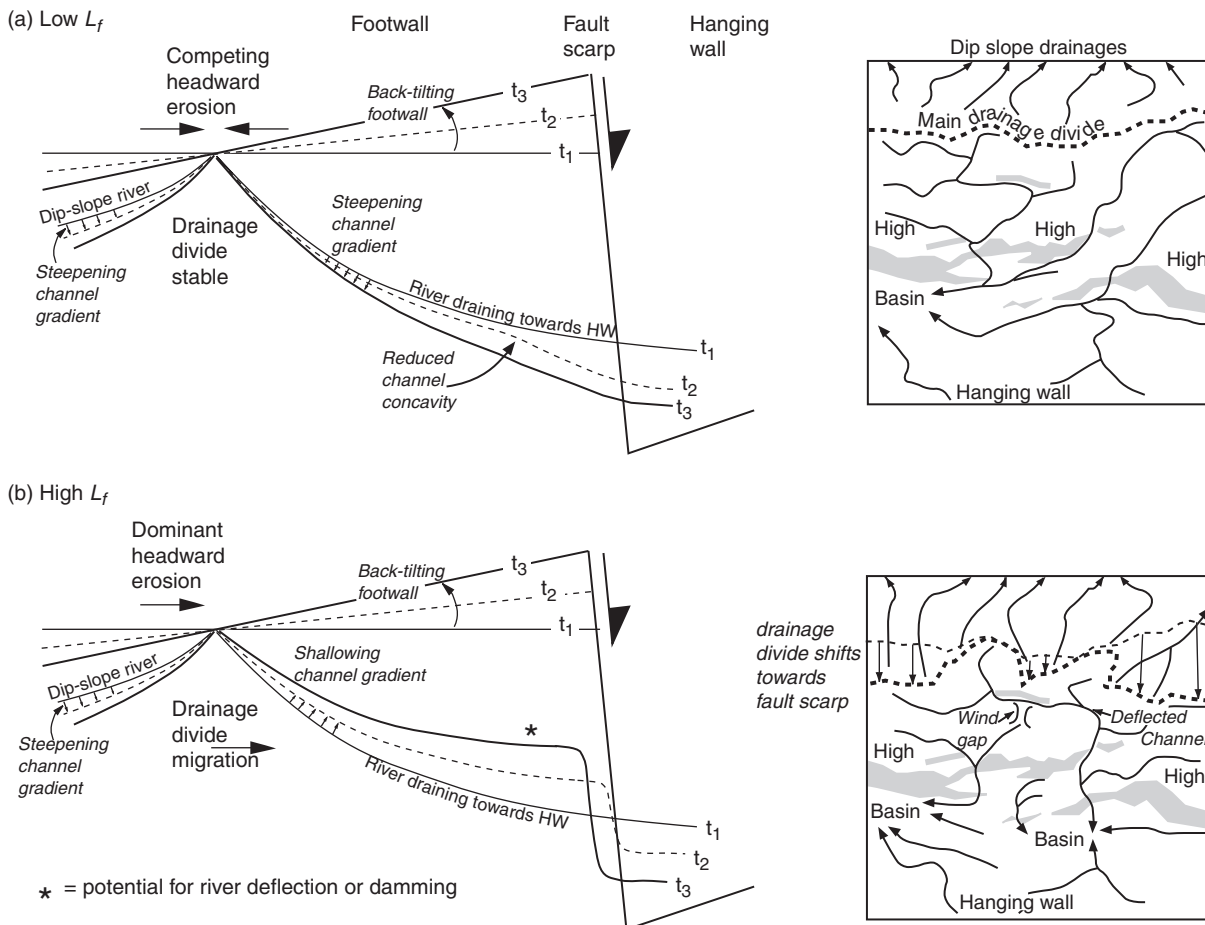


Fig. 16. Diagram summarising river response to fault growth in this model for (a) a low value of  $L_f$ , compared with (b) a high value of  $L_f$ . Line drawings on left hand side show idealised 2D cross-sections from the footwall into the hanging wall of the fault for three different times:  $t_1$  (thin line),  $t_2$  (dashed line), and  $t_3$  (bold line). Map views on right hand side show corresponding fault geometry (grey), rivers (black), and main drainage divide (dashed lines). Back-tilting increases the gradient of channels that drain the dip slope leading to headward erosion. For low  $L_f$  (a), the incision response to fault movement is diffusive (Eqn. (5)) so the gradient of the channel draining across the fault is maintained or steepened as far as the main drainage divide even though the footwall is back-tilting. Competing headward erosion on both sides of the drainage divide leads to a stable divide position along strike and through time. In (b), high  $L_f$ , the incision response to fault movement consists of a 'wave' that migrates upstream with velocity  $\propto 1/L_f$  (Eqn. (4)). Hence the lower reach of the river becomes incised whereas the upper part is back-tilted, reducing headward erosion so the divide may shift closer to the fault scarp along strike and through time. See 'River incision across active fault scraps' and the 'Discussion' for further information.

headward erosion in the hinterland catchments. The former occurs because the dip-slope channels steepen as the footwall is back-tilted, whereas the latter depends on the response of the hinterland catchments to base-level fall at the fault. When  $L_f = 20$  km the main drainage divide is located at a fairly consistent distance of 20–25 km behind the fault scarp indicating that the two rates of headward erosion are similar in magnitude along strike. In contrast, when  $L_f = 100$  km the main drainage divide is highly irregular being only a few kilometres behind the scarp in some places but up to 20 km away in others, which indicates that the two rates of headward erosion differ in relative magnitude along strike (Fig. 15). The rate of headward erosion in the hinterland catchments will also vary over time when  $L_f$  is larger (depending on the velocity of the incision wave) making the divide potentially less stable through time as well. The position of the main drainage divide ultimately determines the drainage area and thus the discharge of

the rivers that drain across the growing scarp into the hanging wall. Figure 15 shows that the available drainage area is generally smaller when  $L_f$  is very large.

By integrating the key features of Figs 14 and 15 we summarise schematically in Fig. 16 the main effects of  $L_f$  on the evolution of river channels that drain across active faults in our model. When  $L_f$  is small, the greater footwall drainage area combined with the rapid upstream migration of incision generated by base-level fall at the fault result in the basinward channel gradient being maintained in spite of the on-going tectonic back-tilt of the footwall. Conversely, when  $L_f$  is large the gradient of the channel upstream of the convex reach is reduced by back-tilting and the upstream drainage area is also reduced in size compared with that when  $L_f$  is small. Thus as  $L_f$  increases the likelihood of a river being defeated or diverted will increase as illustrated by Fig. 16b. We can quantify the threshold where river defeat/diversion will occur by calculating the ratio of

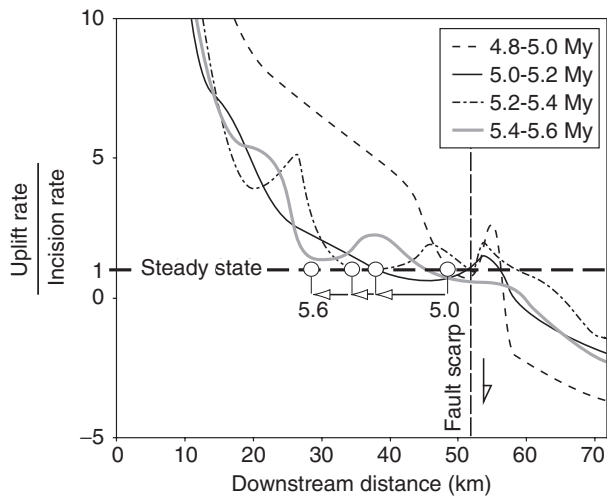


Fig. 17. Ratio of tectonic uplift rate to incision rate as a function of downstream distance along river draining through scarp at locality 2 calculated for four points in time after fault acceleration at 4.6 Myr. Both uplift rate and incision rate are averaged over intervals of 0.2 Myr using the data shown in Fig. 13b and c. Horizontal dashed line indicates topographic steady state *sensu stricto*. Circles indicate the upstream limit of the reach which is in dynamic steady state in the footwall of the fault at each time. Upstream of this limit, uplift rate  $\gg$  incision rate for the four time intervals considered. Note that the zone of dynamic steady state extends further upstream in time (see also Fig. 13b). Downstream of the fault, negative values indicate hanging-wall subsidence that is not balanced by aggradation (See ‘The surface process model’). See ‘Deviation from topographic steady-state in actively incising channels’ for further discussion.

the time required for the incision wave to propagate upstream to a point  $x_p$ , ( $t_{wave}$ ), to the time required to reverse the channel slope at  $x_p$  via back-tilting ( $t_{rot}$ ), i.e.

$$R_t = \frac{t_{wave}}{t_{rot}} = \frac{x_p W L_f (dS/dt)}{Q S_0 K_f} \quad (7)$$

Here we use the wave velocity given in Eqn. (4), and let  $S_0$  be initial channel slope and  $dS/dt$  be tectonic tilt rate at point  $x_p$ . If  $R_t > 1$  (Eqn. (6)), the river draining from a hinterland catchment into the hanging-wall basin will be defeated by the growing fault. Clearly, low gradient rivers (small  $S_0$ ) with small drainage areas (small  $A$  and thus  $Q$ ) incising into resistant lithologies (high  $L_f$ ) across high slip rate seismogenic faults (high  $dS/dt$ ) are therefore more likely to be defeated.

#### *Deviation from topographic steady state in actively incising channels*

Convex profiles (e.g. Figs 13 and 14) are commonly observed in tectonically perturbed channels (e.g. Kirby & Whipple, 2001; Dorsey & Roering, 2006) and are evidence that a river is not in equilibrium with respect to energy dissipation downstream. However, profile convexity does not necessarily mean that a channel is not in topographic steady state, i.e. tectonic uplift rate equal to fluvial incision rate. We can use the output of this model to calculate the

ratio of uplift rate to incision rate at each time step and thus evaluate whether the channel profiles produced using this model reach topographic steady state. Figure 17 shows the results of this calculation using the data presented in Fig. 13b and c. The steady-state condition is indicated by the horizontal dashed line. Clearly none of the curves shown in Fig. 17 follow the steady-state line exactly. However, each curve can be separated into two distinct parts upstream of the fault, identified by the positions of the circles (Fig. 17): Downstream of each circle, at least as far as the fault scarp, the curves fluctuate around the steady-state line (dynamic steady state), whereas upstream of each circle the curves clearly deviate significantly and lie above the line (i.e. uplift rate  $\gg$  incision rate). The section where the channel is in dynamic steady state extends further upstream of the fault over time, indicated by the shift in the position of the circles shown in Fig. 17 (see also Fig. 13b). This shift mirrors the upstream migration of the incision wave shown in Figs 4e–h and 13c (see Discussion above). The main reason why the channel approaches, but never actually achieves, perfect steady state is the episodic nature of fault activity, which arises in the tectonic model due to fault segment interaction (Fig. 7b). Periods of rapid fault slip result in intervals of time when the uplift rate exceeds the incision rate, causing a transient response in channel slope each time an episode of fault movement occurs. In contrast, continuous fault motion (creep) allows a balance between uplift rate and incision rate to be established and then maintained, once the initial transient response to fault initiation has ended, because there is no further variation in tectonic forcing. This explains why the convex reach is less pronounced for the case of uniform fault slip rate (Fig. 14b), i.e. more of the river reach up stream of the fault is at or approaching steady state in the case of uniform uplift rate after 4.6 Myr, compared with the episodic case in which the river continues to be irregularly forced after 4.6 Myr.

## DISCUSSION

The focus of this study has been to understand how the transition from a diffuse array of active fault segments to the formation of a major through-going linked structure impacts the size of footwall catchments, the location and persistence of sediment entry points from the footwall into the hanging-wall basin, and the variations in sediment volume and yield in space and time. The significance of the transition in structural style is that the spatial organisation of the fault pattern is closely related to changes in the rate of fault slip: as the degree of along-strike continuity of the footwall scarp changes, the rate of footwall uplift, and thus relief across the fault, increases. We have been able to show explicitly that this structural evolution plays a key role in the development of large footwall catchments ( $\gg 100 \text{ km}^2$ ) and, moreover, determines the characteristics of these sediment source areas through time. We now compare our results to real examples, review the basis for

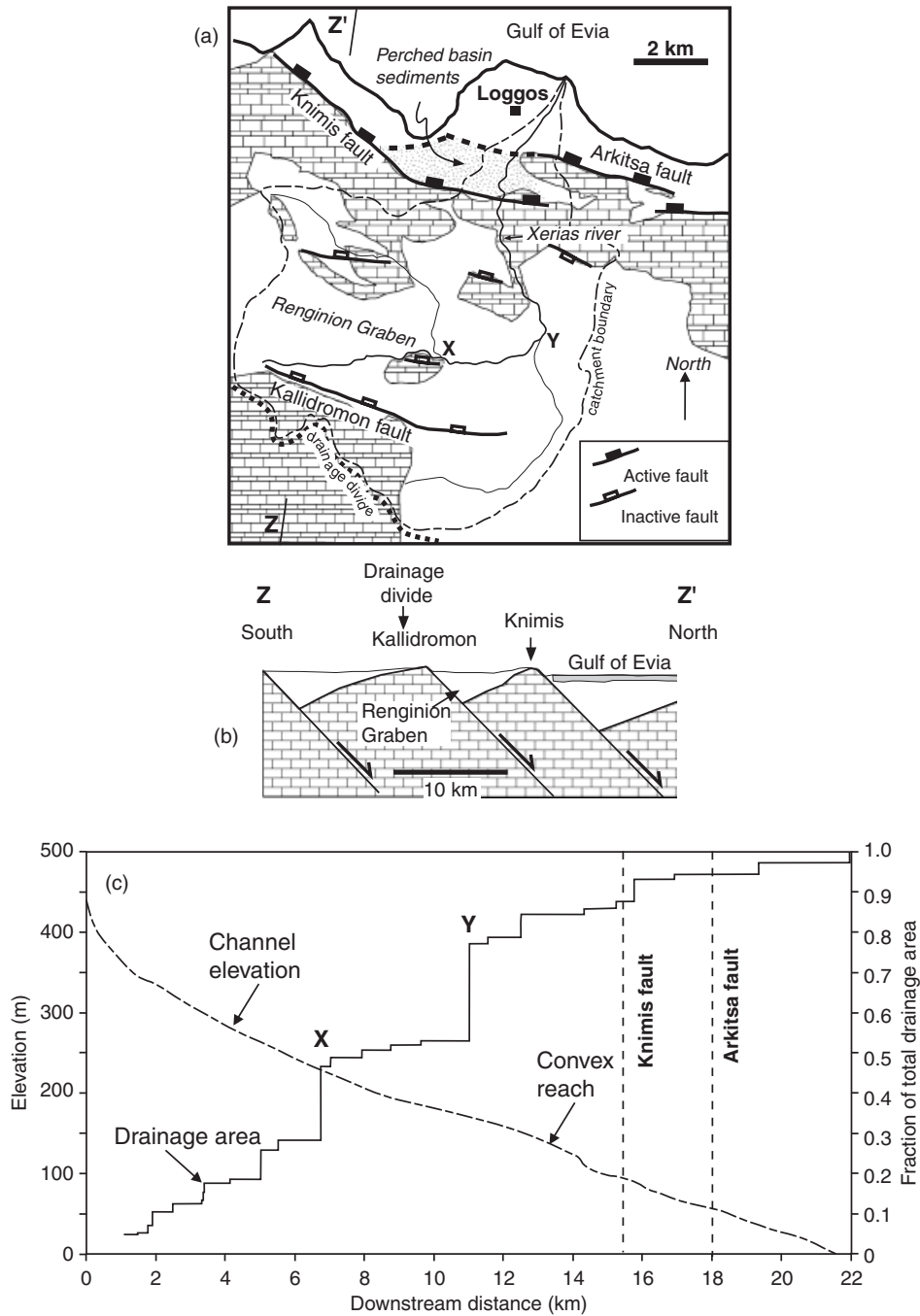


Fig. 18. (a) Map the Xerias catchment in the Renginion graben on the southern margin of the Gulf of Evia in mainland Greece, showing the geometry and extent of the catchment and the main drainage channels. Outcrops of Mesozoic limestone indicated by block pattern; white areas show Neogene basin fill. (b) Schematic structural cross-section (Z-Z') across the basin from south to north. (c) Channel elevation and drainage area as a function of downstream distance for the Xerias river, obtained from a 20 m DEM. Elevations ground-truthed using barometric spot heights where DEM errors were large. Points X and Y are located on map (a). See 'Drainage network evolution in extensional settings' for discussion.

the main assumptions of this study and discuss some implications for interpreting field data.

### Drainage network evolution in extensional settings

The results from the coupled model show how each stage of fault array growth contributes to catchment development. The initially diffuse pattern of faulting with slow

rates of fault growth allows large drainage basins to develop while the topographic relief is low and the fault scarps are of limited lateral extent. As fault interaction begins, some footwall areas begin to grow preferentially and develop steeper displacement gradients at their tips. Dip-slope drainage patterns begin to develop on the footwall highs with locally fault-parallel drainage channels developed in the tip region. As the pattern of faulting is still distributed at this stage, these fault parallel channels can flow along-

strike from the footwall of one fault into the hanging wall of a neighbouring segment, leading to extensive river reaches that flow axially through the fault array and are sensitive to variable rates of slip along different segments (e.g. Trudgill, 2002). The combination of fault parallel and fault perpendicular flow leads to trellis drainage networks that are characteristic of active rift settings (Fig. 9; Ollier, 1981; Eliet & Gawthorpe, 1995). The drainage network becomes unstable at this stage in our model as channel gradients are perturbed locally by faults, resulting in deflection and/or damming. However, with continuing fault interaction many of the early-formed fault segments become inactive and the deformation becomes localised onto a few, large, rapidly growing faults. These high-slip-rate faults control local base level across large areas of the fault array and the early-formed catchments become uplifted as the areal extent of footwall uplift increases. This is the time interval where maximum instability in the drainage network is observed as competing rates of uplift and subsidence on adjacent, strongly interacting, fault segments leads to headwater capture between neighbouring drainage basins.

Once segment linkage occurs, the drainage network stabilises. The stabilisation is largely due to river incision into the growing footwall scarp, driven by the increased slip rate on the linked fault. However, stabilisation of the drainage pattern is also due to the fact that spatial variation in fault slip rate diminishes after segment linkage (Cowie *et al.*, 2000). The resulting landscape consists of a prominent through-going fault scarp, which separates a laterally continuous back-tilted footwall high from a laterally extensive hanging-wall depocentre. A particularly important result is that the main drainage divide is located a considerable distance into the footwall block, of the order of  $10^4$  m behind the scarp. For this particular model the distance is 15–20 km, which is approximately half way between the largest-scale faults ( $\sim 40$  km). This distal location is established during the early diffuse stage of fault activity and only migrates by a relatively small amount (a few kilometres in our model) due to headward erosion during subsequent fault array evolution. Because of the distal location of the main drainage divide, the large drainage basins within the footwall area are maintained, i.e. become locally antecedent, and supply the hanging-wall depocentres throughout their development.

We suggest that trellis drainage patterns in extensional settings can reveal the spatial extent of active faulting during early stages of the rifting history. For example, Eliet & Gawthorpe (1995) document excellent examples of trellis drainage networks within the Neogene Renginion graben, along the southern margin of the Gulf of Evia in mainland Greece. The faults that bound the southern margin of the Renginion basin, the Kallidromon fault array, are now inactive and are being uplifted in the footwall of active normal faults that define the coastline, the Knimis–Arkitsa fault array (Roberts & Jackson, 1990; Eliet & Gawthorpe, 1995; Goldsworthy & Jackson, 2001; Fig. 18). The present day slip rate on the Knimis fault is estimated to be

$1\text{--}2\text{ mm yr}^{-1}$  (Ganas, 1997; Goldsworthy & Jackson, 2001). Goldsworthy & Jackson (2001) argue that the Knimis–Arkitsa fault array is younger than the Kallidromon fault array by  $\sim 1\text{--}2$  Myr, and that it formed independently. However, their field data cannot exclude the possibility that they initiated at approximately the same time as segmented arrays that have been interacting as they evolved; i.e. the cessation of activity on the Kallidromon fault array may have coincided with increased rates of slip on the Knimis–Arkitsa fault array as it began to link, similar to fault array evolution seen in other rift basins (e.g. Gawthorpe *et al.*, 2003; Cowie *et al.*, 2005). One of the outcomes of our modelling study is that we have been able to show that the presence of these trellis drainage networks is a strong indication of such across-strike fault interaction (cf. Figs 8 and 9). Moreover, the position of the drainage divide in the footwall of the Kallidromon fault array,  $\sim 15$  km to the south of the Gulf of Evia, is also consistent with the interpretation that the two fault arrays have been interacting as they evolved.

The Xerias river, which drains a large part of the Renginion graben, provides a good example of a drainage network that we can compare quantitatively with data extracted from the model (Fig. 18). This river supplies sediment to a large fan-delta in the Gulf of Evia and has a drainage area of  $98\text{ km}^2$  (Ganas, 1997). A significant proportion of the headwaters of this river drain south down the dip-slope of the Knimis fault block, then combine to form rivers that flow parallel to fault strike (eastward) (point X; Fig. 18a) and ultimately turn northward before crossing the active Knimis fault scarp near Loggos. This is a classic example of a trellis network and is very similar to those which develop within our model (e.g. Fig. 13). Figure 18c shows channel elevation and drainage area as a function of downstream distance for the Xerias river. Point Y is highlighted because this is where the river turns to flow north across the back-tilting footwall of the Knimis fault. This point is located at  $\sim 50\%$  of the total downstream distance in this catchment. Most of the drainage area of the catchment ( $\sim 80\%$ ) lies upstream of point Y, whereas along the reach where the river is incising across the footwall uplift there is only a small downstream increase in drainage area (Fig. 18c). Furthermore, between point Y and the Knimis fault scarp the channel profile becomes convex, whereas upstream of Y the profile is concave. All of these features are similar to those observed for rivers draining across active faults in our numerical model (e.g. Figs 13 and 14) and are evidence that fault growth is exerting a strong control on the drainage network in this area of the Renginion basin, as Eliet & Gawthorpe (1995) proposed.

There are several lines of evidence which suggest that the point where the Xerias river enters the Gulf of Evia was, at some point in the past, a displacement minimum between the Knimis and Arkitsa fault segments that have since linked. There is a prominent offset, or 'step', in the surface trace of the Knimis–Arkitsa fault array near Loggos, within which basin sediments are exposed that are

perched above adjacent hanging-wall stratigraphy (Roberts & Jackson, 1991). This stratigraphic geometry is characteristic of a breached relay ramp between two extensional fault segments. The convex river profile upstream of the fault is evidence that there is now a through-going active fault scarp that is perturbing this channel. Our modelling study, and in particular the model results shown in Fig. 14, lead to the conclusion that the convexity started to develop at the time of segment linkage, i.e. 1–2 Ma.

### Controls on fluvial incision across growing footwall uplifts

In ‘The surface process model’ and ‘Results derived from the coupled model’ we explain the factors that control the incision rate of the fluvial channels in this model and thus what determines whether a river is able to maintain its course across a growing footwall uplift (‘Influence of varying  $L_f$ ’). Clearly our assumption that channel width,  $W$ , is constant has a major influence on the incision rate. This assumption is based on field observations, summarised in Fig. 3, and on the fact that the empirical scaling relationship  $W \propto Q^{0.5}$  is probably inappropriate for channels that drain areas of complex active faulting such as that generated by the fault growth model (‘Hydraulic geometry – channel width,  $W$ ’). To investigate this further we conducted a parameter study in which we allowed for a dependence of channel width on discharge, i.e.  $W \propto Q^\phi$  with  $0 \leq \phi \leq 0.5$ , and we varied  $K_f$  over six orders of magnitude and  $L_f$  over the range  $dx \leq L_f \leq 100$ . We found that when  $\phi > 0$  no major rivers systems developed that drained from the footwall into the hanging wall, which is clearly unrealistic as shown by the field examples (Figs 3 and 18). Varying  $K_f$  and  $L_f$  did not modify this basic result; the drainage patterns obtained were consistently characterised by flow directed down the footwall dip-slope rather than across the fault into the hanging wall, and numerous lakes formed as drainages were dammed behind growing fault scarps. Also the main drainage divide was consistently located a small distance behind the scarp, similar to the result shown in Fig. 8b. In our view, allowing channel width to be independent of drainage area in our modelling approach actually leads to more realistic landscapes.

It seems clear from the above results that we need to develop a much better understanding of the factors that control channel width for rivers that drain through areas of active tectonic uplift. In some field examples width appears to scale with drainage area, although the scaling exponent may vary with uplift rate (e.g. Duvall *et al.*, 2004), whereas in other cases the relationship appears to break down (e.g. Fig. 3). Wohl (2004) argues that hydraulic scaling in bedrock rivers breaks down if the ratio of total stream power to the coarse grain sediment fraction (characterised by  $D_{84}$ ) is  $\leq 10^4 \text{ kg s}^{-3}$ . If the ratio is below this threshold it may indicate that the hydraulic driving forces are insufficient to adjust channel form because of the high erosional resistance of the substrate (Wohl, 2004). The rivers that in-

cise across the active faults in our model do generate landslides along the valley sides (Fig. 4). In nature this process may feed coarse material directly into the channel, which could, potentially, increase the value of  $D_{84}$ . Landslides can also emplace large, immobile blocks in the channel that will increase channel roughness and decrease flow velocity, and may also result in a decrease in stream power. To assess the importance of these factors in controlling channel width in tectonically active areas, grain size data are required where rivers are incising across active faults with known uplift histories. Whittaker *et al.* (in press) argue for an alternative explanation for the breakdown in hydraulic scaling which is that it is an intrinsic characteristic of rivers undergoing a transient response to tectonic forcing, consistent with the scenario simulated by our model (see also Wobus *et al.*, 2006).

We showed in ‘Influence of varying  $L_f$ ’ that the parameter  $L_f$  controls the nature of the incision wave that migrates upstream from the fault when the fault slip rate increases. This parameter controls valley form through its effect on intrinsic concavity (Eqn. (3)), but more importantly the velocity of the incision wave scales as  $1/L_f$  (Eqn. (4)). Thus, when  $L_f$  is small the velocity is high and in the limit that  $L_f \rightarrow dx$  (the TL end member) the entire footwall catchment instantaneously feels the effect of a base-level fall (see also Whipple & Tucker, 1999). The consequence of this is that a river draining across a back-tilting fault block is much more likely to maintain its course if it is close to being transport limited ( $Q_s \approx Q_c$ , erodible substrate; Fig. 16a). As a river becomes progressively more under-supplied (larger  $L_f$ ;  $Q_s < Q_c$ , more resistant substrate) it is more likely to be deflected or dammed by the growing fault mainly because the velocity of the incision wave will be correspondingly slower (Fig. 16b). In the latter case, the rate of tectonic back-tilt may be sufficient to reverse the gradient of the river upstream of the fault, especially if the initial gradient of the river is fairly low (Eqn. (6); Fig. 16b).

The long profiles of the Rio Torto (Fig. 3b) and the Xerias river (Fig. 18b) are strikingly similar to those shown in Fig. 14a. In the case of Xerias river, we infer that the convex river reach developed in response to a fault linkage event 1–2 Ma, whereas in the case of the Rio Torto the profile convexity can be attributed to a known increase in fault slip on the Fiamignano fault which occurred  $\sim 1.0$  Ma (Roberts & Michetti, 2004). In both examples the rivers are down-cutting into Mesozoic limestone exposed in the footwalls of active normal faults and have maintained their courses in the face of tectonic back-tilting. If we interpret these field data in terms of the fluvial incision model used here it implies that the Rio Torto is strongly under-supplied and thus very close to the end member of DL river incision. The convex reach on the Xerias river is much less pronounced. The simplest, although not the only, interpretation of the difference is that the presence of easily erodible Neogene sediments in the upper part of the catchment means the Xerias river is not as strongly under-supplied as the Rio Torto. This interpretation is also consistent with the recent modelling results of Gasparini *et al.* (2006).

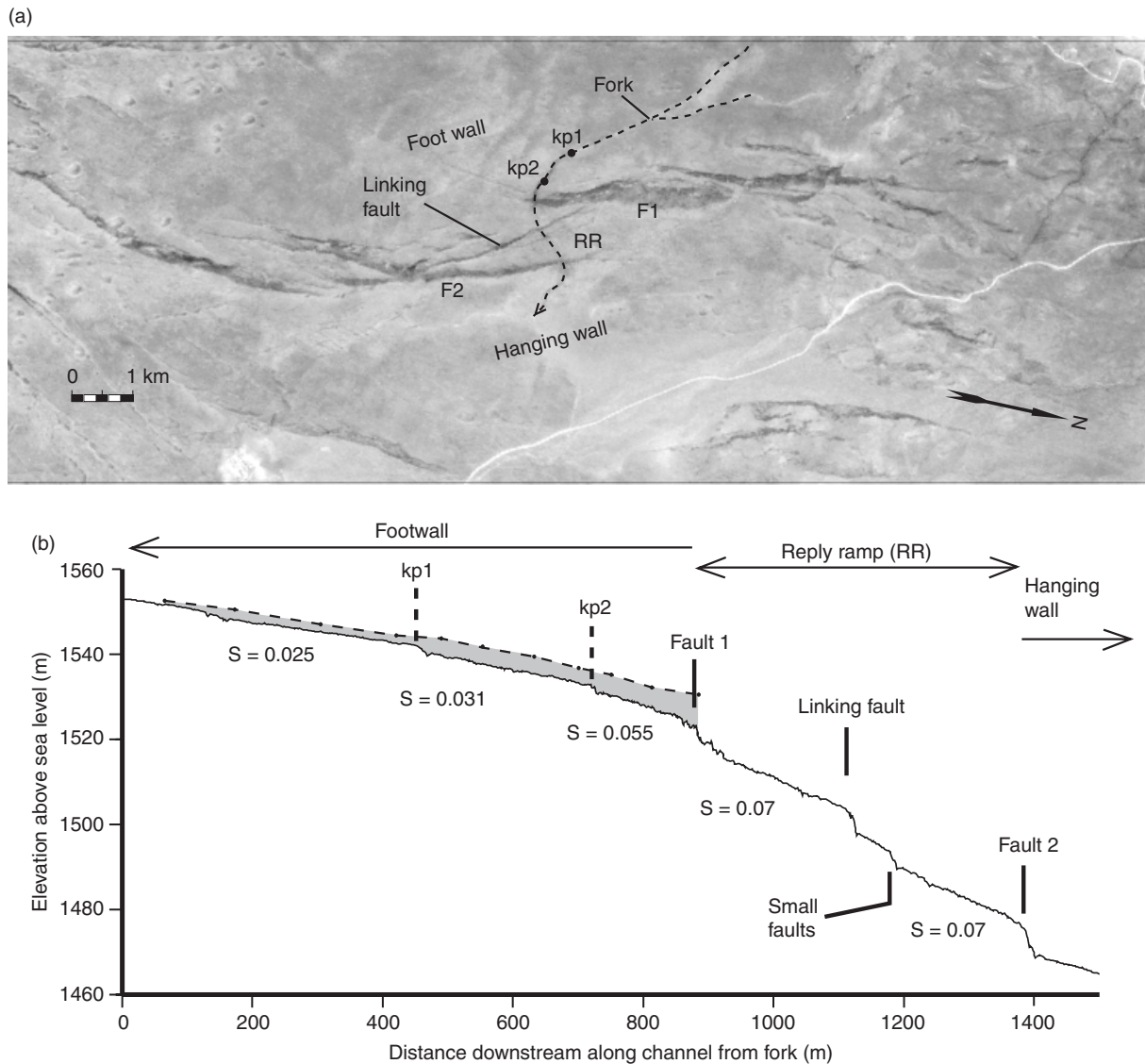


Fig. 19. (a) Aerial photo showing an extensional fault array in the Volcanic Tableland, E. California mapped by Dawers and Anders (1995). The fault consists of several segments separated by relay ramps, the largest of which is marked RR. F1 and F2 refer to the two fault segments (faults 1 and 2) on either side of this relay ramp. The total length of the array is  $\sim 7$  km and the maximum throw is  $\sim 95$  m. (b) Long profile of the stream channel that drains across this fault and down the relay ramp (RR) between fault segments, F1 and F2. The location of the stream is marked by a dashed line in (a) and two prominent knickpoints upstream of the fault, kp1 and kp2, are marked by dots. The channel slope,  $S$ , is indicated by the numbers below the profile and the grey shaded area gives a minimum estimate of the total amount of vertical incision (see Gilpin (2003) and 'Controls on fluvial incision across growing footwall uplifts' for further details).

Figure 19 presents a field example that helps to explain how the convex reaches on the Xerias and Rio Torto river profiles may have been formed. This example, from the Volcanic Tableland in Eastern California, shows a convex long profile from a stream channel draining across a normal fault in the 0.76 Ma Bishop Tuff (Gilpin, 2003). Two knickpoints (kp1 and kp2) are evident upstream of Fault 1, separated by channel reaches which have approximately constant gradients (Fig. 19b). Gilpin (2003) argued that the knickpoints were generated by tectonic movement on Fault 1 and migrated upstream, primarily by progressive detachment of blocks of tuff. Upstream of the highest knickpoint (kp1), the average gradient,  $S \approx 0.025$ . Between kp1 and kp2,  $S$  increases to  $\sim 0.031$  and between the fault

scarp (Fault 1) and the lowest knickpoint (kp2)  $S$  again increases to  $\sim 0.055$  (Fig. 19b). The grey shaded area in Fig. 19b shows a minimum estimate of the total amount of vertical incision of the channel into the tuff surface across the footwall of the fault since 0.76 Ma. The total amount of vertical incision clearly increases towards the fault. Both the convex river profile upstream of Fault 1 and the increase in incision towards the fault in this example appear to have been produced by the upstream migration of a sequence of knickpoints that originated from slip events on Fault 1. The top of the convex reach is interpreted to mark the position of the oldest knickpoint in this scenario, formed at the time of fault initiation. Although individual knickpoints are clearly not resolved by the profiles shown

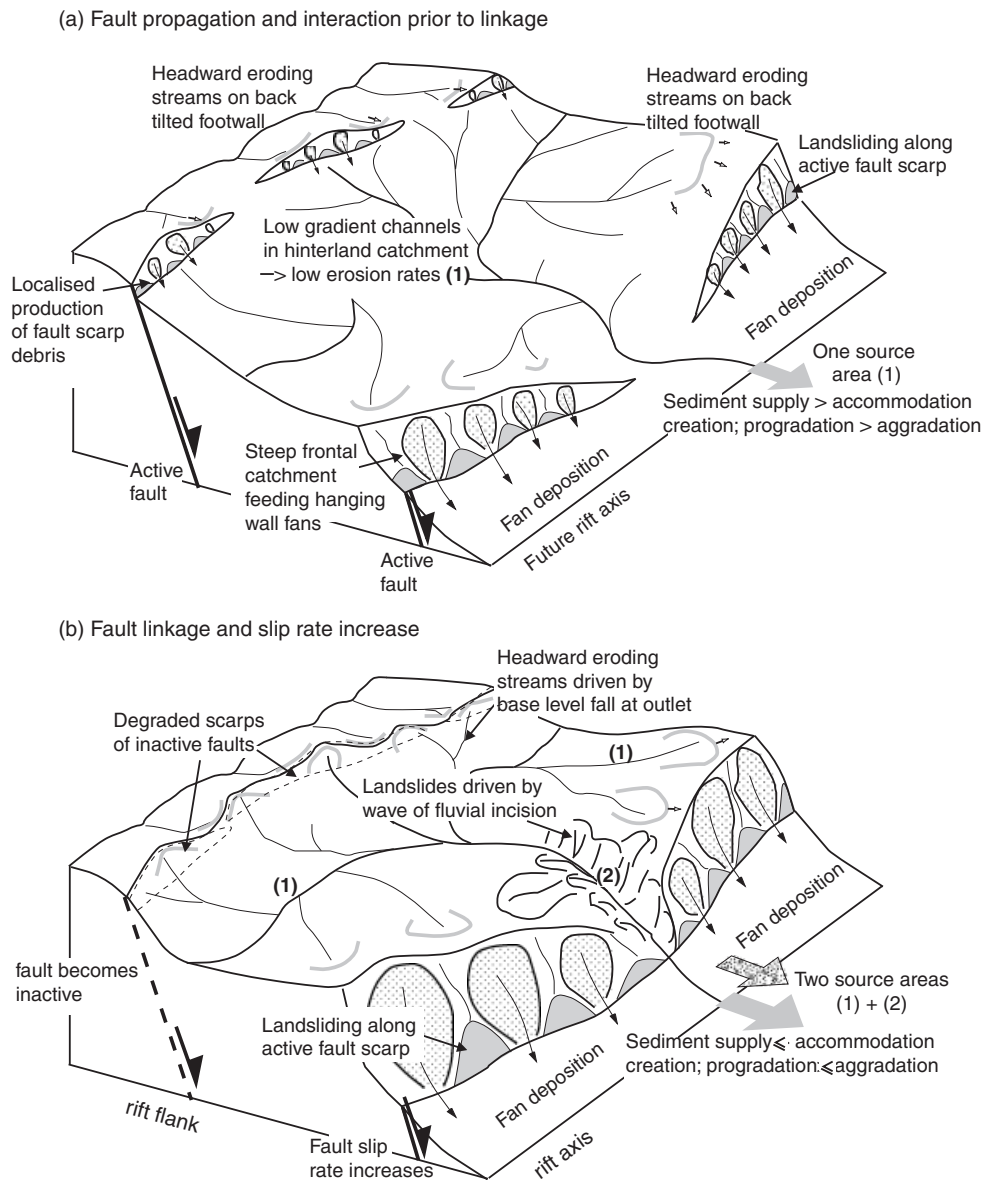


Fig. 20. Schematic diagrams summarising the main features of the model behaviour: (a) relates to the early rift-initiation phase and (b) relates to the late rift-initiation (see text for discussion).

in Figs 3b and 18b, it is reasonable to argue more generally, based on our modelling results, that if  $Q_s \ll Q_c$  episodic fault slip will drive successive pulses of incision upstream (Fig. 17) and a convex river profile will gradually develop (Fig. 13b).

### Nature of sediment supply variations associated with fault interaction and linkage: implications for syn-rift stratigraphic patterns

Gupta *et al.* (1998) suggested that the changes in fault slip rate associated with segment linkage to form a through-going basin-bounding fault can explain the rift-initiation to rift-climax transition observed in most rift basin successions. The transition occurs when the rate of basin subsidence changes from being relatively low, and sedimentation keeps pace with subsidence, to when subsi-

dence rates are high and outpace sedimentation (Prosser, 1993; Lambiase & Bosworth, 1995). Facies variations associated with this transition have previously been viewed largely from the perspective of changing accommodation creation rather than explicitly considering the surface process response of footwall catchments to growth of the extensional fault system. In this section we use the results of our modelling study to predict likely variations in sediment supply to a growing rift basin as the along-strike continuity of the footwall scarp increases, and the rate of footwall uplift, and hence relief across the fault, increases (Fig. 20).

#### Early rift initiation

We find that during the initial diffuse stage of fault development, low-gradient rivers are established that are able to exploit the numerous gaps between fault segments to

supply sediment to hanging-wall depocentres. In addition to this structural control of plan view channel geometry, we show that the headwaters of many of these rivers are draining down the dip slopes of actively growing footwalls so that channel gradients become steeper due to tectonic back-tilting (Fig. 20a). This results in a gradual increase in the volume of sediment supplied by these rivers over time and the increase begins during the earliest phase of extensional fault development. During this phase, the rate of hanging-wall subsidence is relatively low and the depocentres are initially very shallow (e.g. Cowie *et al.*, 2000).

The large drainage areas of these low gradient catchments, combined with increasing sediment supply, the large number of pathways for fluvial systems to develop and low rates of tectonic subsidence, means that it is relatively easy for sedimentation supply to keep pace with accommodation creation in individual depocentres. The sediment input is likely to be relatively mature (i.e. well-processed by the fluvial system) and consist of a well mixed assemblage of the more weathering-resistant lithologies over an area of several hundred km<sup>2</sup> ('Sediment supply variations from footwall catchments in space and time'). Coarse debris, derived from erosion within small (< 10 km<sup>2</sup>) scarp front catchments, may accumulate locally in the immediate hanging wall of the most active fault scarps.

With this interpretation in mind, it is straightforward to explain the characteristics of the early rift-initiation phase of extensional basin development, which is typically characterised by fluvial and, locally, lacustrine facies with sedimentation rates approximately equal to the rate of tectonic subsidence (e.g. Gupta *et al.*, 1998; Cowie *et al.*, 2000; Sharp *et al.*, 2000). It is also easy to understand why antecedent drainage patterns are often invoked to explain early syn-rift deposits. In our model all the drainage patterns are contemporaneous with faulting but they initially have the characteristics of regionally extensive, low gradient drainage basins that can potentially transport unique lithologies from areas well away from where the main extensional deformation eventually takes place. Thus, although antecedent drainage clearly must play a role in drainage network formation, our modeling suggests that it does not need to be invoked to explain the nature of early syn-rift deposits.

#### *Late rift initiation*

In the tectonic model used here, the onset of strong fault interaction leads to increased rates of fault slip along the largest, fastest growing fault segments (Fig. 20b). This is when landslides first occur in this study and they are initially confined to the centres of long fault segments where both the throw and throw rate are high. Sediment volumes from the footwall catchments begin to increase significantly during this phase. We also find that sediment yield for these catchments is spatially very variable depending on where the catchments are located with respect to areas of rapid footwall uplift (Fig. 10). Catchments which develop in the immediate footwall near the centre of large,

high slip rate, fault segments are characterised by high sediment yields, steep channel gradients and short transport distances into the basin. Other catchments, located in areas of lower fault throw and slip rate, may be spatially more extensive and produce a greater volume of sediment but they are characterised by relatively low sediment yield, low channel gradients and long transport distances. The sediments derived from adjacent catchments along the linking fault array may be quite distinct because of this structural control. The high-yield catchments are likely to produce more angular, less well sorted material, possibly coarser and compositionally dominated by fault scarp lithologies, whereas the input to the basin from the low-yield catchments is likely to be sedimentologically more mature and compositionally similar to the fluvial input of the early rift initiation ('Early rift initiation').

Some fault segments have begun to link at this time, so that the number of structural gaps in the fault trace is diminished. However, this does not necessarily reduce the number of sediment entry points to the basin as many rivers continue to drain across active fault scarps (Fig. 20b). Thus although the segmented nature of the faults clearly influences the early drainage pattern, persistent segment boundaries do not necessarily play an important role as the fault array evolves. For example, we see that one of the largest footwall catchments (i.e. (ii); Fig. 6) consistently drains through a small relay zone between two fault segments that linked relatively early (4.6 Myr), whereas the adjacent catchment (i.e. (iii); Fig. 6) is smaller, even though it drains through a relay zone that is more than twice as big and persists as a clear segment boundary until much later in the fault evolution (5.6 Myr). Rivers that maintain their course across a fault where linkage has recently occurred are predicted to supply detritus comprised of two components with distinct sedimentary character: the dominant component is produced by relatively low rates of erosion over most of the upper part of the catchment whereas the other component is derived from areas in the proximal footwall as the erosion rate increases in response to increased fault throw and slip rate (Fig. 20b). The formation of longer fault segments, combined with more rapid subsidence rates in their hanging walls, also leads to stronger structural control in the routing of rivers in the hanging-wall area. We also see that phases of episodic slip on adjacent fault segments can result in deflection of fluvial channels so that the sediment supply may be temporarily diverted into a different sub-basin.

Given the above factors, we expect the late rift-initiation phase to show the greatest lateral variability in sediment facies, with abrupt facies shifts both spatially and through time. Facies variability very similar to what we predict here has been documented within the early syn-rift succession of the Gulf of Suez by Sharp *et al.* (2000) and Gupta *et al.* (1999). Although these facies patterns were inferred to have been caused by differential fault growth and fault segment interaction within the evolving Gulf of Suez rift, the causal relationship had not been demonstrated.

*Rift initiation to rift-climax transition*

The final phase that we recognise occurs as the fault array becomes fully linked and the slip rate is both higher and more uniform along fault strike. We relate this phase to the onset of the rift climax, during which major extensional fault systems emerge and many of the early-formed faults are no longer active. In our model, there are two important changes to the catchment geometry and the sediment supply associated with this transition. Firstly the drainage geometry stabilises, and secondly there is a greater component of material derived from rapid incision into the uplifting footwall. Thus we infer that major focused sediment supply routes to the basin become established during this phase. The sediment supply increases through time as the fault slip rate increases and the calibre of the sediment is also predicted to change as the region immediately upstream of the scarp becomes more deeply incised ('Sediment yield variations through time for a single footwall catchment'). In particular, in our model, this interval of time is generally associated with high erosion rates and land slides along steep slopes that flank incised channels in the footwall area. In nature, the landslide debris may be fluvially reworked and transported into the basin leading to an influx of coarser, less well-sorted material. The influx of coarse material, combined with the increased rate of accommodation creation in the proximal hanging wall, may explain the formation of vertically stacked fan deltas along rift basin margins during the mid to late syn-rift, e.g. the Miocene Alaqa delta complex in the Gulf of Suez (Gupta *et al.*, 1999; Sharp *et al.*, 2000).

Traditionally the rift-climax phase is recognised as the period of time during which tectonic subsidence rates are high and outpace sedimentation rates. The degree of sediment starvation associated with this transition must be partly controlled by the response of the fluvial system to increased rates of uplift in the footwall (or basin margin) area. In our model we investigated a wide range of values of the parameter,  $L_f$ , to simulate fluvial systems that range from being strongly under-capacity ( $Q_s \ll Q_c$ ;  $L_f$  large; resistant lithology), to being close to capacity ( $Q_s \approx Q_c$ ;  $L_f$  small; highly erodible lithology). For small  $L_f$ , the change in fault slip rate associated with fault linkage results in incision that very rapidly affects the full extent of the footwall catchments up to the drainage divide. In contrast, when  $L_f$  is large the same slip rate change generates an incision response that propagates much more slowly so that  $\sim 1.0$  Myr after fault acceleration fluvial incision is still focused immediately upstream of the scarp and most of the drainage area of the footwall catchments is unaffected.

In the light of these results, we suggest that if a basin is supplied with sediment via fluvial systems that are 'transport limited' the basin fill may be less likely to show abrupt change in facies and/or sediment starvation associated with the rift-initiation to rift-climax transition. The facies change is likely to be much more obvious in a basin that is supplied by river systems that are strongly under-capacity (i.e. DL). This effect may be accentuated by the fact that a

high value of  $L_f$  increases the likelihood of rivers being deflected or dammed by the growing fault ('Influence of varying  $L_f$ ').

**SUMMARY AND CONCLUSIONS**

A large body of theoretical work exists which predicts how extensional faults evolve in the brittle crust and how these faults control accommodation creation in rift basins (e.g. see Gupta & Cowie, 2000 for a review). In contrast, relatively little theoretical work has been published to date which aims to demonstrate how the growth of these same faults influences surface processes occurring within the uplifted footwall that borders the basin. Consequently, research into the stratigraphic development of rift basins generally relies heavily on hypothetical scenarios derived from field observations (e.g. Gupta *et al.*, 1999; Gawthorpe & Leeder, 2000). Here we have presented the first attempt to couple a landscape evolution model, CASCADE (Braun & Sambridge, 1997), to a tectonic model that is based on fundamental principles of rock physics and reproduces realistic patterns of fault nucleation, propagation, stress interaction and segment linkage on a regional scale ( $> 100$  km). Our main aim has been to understand how the temporal evolution of an extensional fault array influences drainage network development and river incision within the uplifted footwall area, the spatial and temporal distribution of landslides, and the delivery of sediment from the fault-bounded basin margin into the adjacent hanging-wall basin.

We first derive a process-based explanation for the 'fluvial length scale',  $L_f$ , used in the 'under-capacity' model for fluvial incision implemented within CASCADE. (Appendix A). Specifically, we show that  $L_f = q_c/D_c$ , where  $q_c$  is sediment transport capacity per unit flow width,  $D_c$  is the detachment capacity under clear-water flow. By substituting expressions for  $q_c$  and  $D_c$ ,  $L_f$  can then be recast in terms of erodability of the substrate. To provide additional constraints on the fluvial incision algorithm we present new channel geometry data from a river draining across an active normal fault (Fig. 3), which show that high flow channel width does not scale with drainage area in a zone of active normal faulting. Using this model we have reached the following conclusions:

(1) *Position of the main drainage divide relative to the basin margin and the characteristics of footwall catchments:* The most significant and consistent result of this study is the distal position of the main footwall drainage divide relative to the scarp of the basin-bounding fault. For this particular model the distance is 15–20 km, which is approximately half way between the largest-scale faults that develop ( $\sim 40$  km). This distal position is the direct result of fault interaction effects, in particular across-strike interaction during the early diffuse stage of fault pattern development. We can therefore explain for the first time a feature that is commonly observed in active rift settings, without having to invoke pre-existing drainage patterns. More impor-

tantly, the distal position of the drainage divide permits large footwall catchments ( $\gg 100 \text{ km}^2$ ) to develop that can supply significant sediment volumes to the adjacent hanging-wall depocentres throughout the entire evolution of the fault array. These catchments, which we refer to as *hinterland catchments*, have previously been interpreted as antecedent drainages, whereas we have shown that they can arise contemporaneously as a natural response to fault array growth. The drainage areas of hinterland catchments are found to be controlled by the temporal evolution of the regional fault pattern, not just the size, geometry and longevity of the relay ramps through which they drain into the basin. We also show how the trellis drainage networks, which generally characterise these hinterland catchments, result from across-strike fault interaction and compare well with drainage networks observed in areas of active extension in mainland Greece. The scaling of drainage area with downstream distance in trellis networks influences the incision rate of these rivers in the crucial area where they incise across (or become defeated by) relay breaching fault(s) (see conclusion 3).

2) *The timing and source area characteristics of sediment input to rift basins*: We find that the total sediment volume produced by a footwall catchment through time depends on its drainage area, but sediment yield and erosion rate depend on the catchment's position relative to the maximum fault throw and throw rates, as Densmore *et al.* (2003) showed. Catchments that develop in the immediate footwall of large early-formed fault segments produce lower volumes of sediment, but exhibit high yields and erosion rates and show only minor variations in drainage area as the fault pattern evolves. In contrast, catchments which develop and discharge across the fault in areas where the *variations* in throw and throw rate are greatest, i.e. zones of strong fault interaction and incipient linkage, show significant variations in drainage area due to drainage capture. Hence the sediment volumes produced, as well as the yields and erosion rates are very variable across these catchments.

As the size and elevation of the footwall areas increase the sediment volume delivered to the hanging-wall basin increases. Our study shows that the timing of the increase in sediment volume is sensitive to the spatial extent and location of headwaters relative to growing footwall highs across the entire catchment, and may not directly reflect the degree of fault development where the river enters the basin, emphasising the importance of understanding the three-dimensional nature of the uplift field for predicting sediment supply variations in rift settings. The increase in slip rate associated with fault segment linkage generates a wave of fluvial incision that migrates upstream from the linked fault scarp towards the main drainage divide. This response results in a change in sediment yield and erosion rate across the footwall catchments as a function of time, potentially associated with hill-slope failure (i.e. landslides) along valley sides. If the rivers draining the footwall are detachment limited, the relative increase in sediment volume generated by the slip rate acceleration is less

pronounced than it is when the rivers are transport limited. Moreover, DL rivers are more susceptible to damming and drainage reversal upstream of the fault scarp (see conclusion 3). These two effects mean that accommodation creation is more likely to exceed the sediment supply from DL fluvial systems, resulting in sediment starvation associated with abrupt lateral and vertical facies changes.

(3) *Evidence for fluvial incision processes in rivers draining across the footwall of active normal faults*: We find that the diffusive response of TL river systems to base-level fall at the fault means that a basin-ward channel gradient is maintained in the face of the tectonic back-tilt of the footwall. The resulting river profiles are characterised by low concavity or weakly convex reaches upstream of the fault. In contrast, rivers that are strongly under-supplied, or 'DL' respond to base-level fall by focusing incision initially at the fault while the upper reaches of the catchment are passively back-tilted. The resulting river profiles in this case are characterised by prominent convex reaches immediately upstream of the fault whereas channel gradients in the headwaters may be anomalously low and susceptible to reversal or damming. In general the modelled rivers are not in topographic steady state *sensu stricto* (fluvial incision rate  $\neq$  tectonic uplift rate). However, a zone of dynamic steady state develops first where the channel intersects the active fault and extends upstream from the fault scarp driven by the wave of fluvial incision. Channel geometry and hill-slope processes change most dramatically through time at the upstream edge of the wave which coincides approximately with the top of the convex reach.

These results are used to interpret the long profiles of rivers incising across the footwalls of active normal faults in central Italy and mainland Greece. Both river profiles show convex reaches upstream of the fault and have been perturbed by an increase in fault slip rate in the last 1–2 Myr. Field data from the Volcanic Tableland in eastern California provide evidence of the specific mechanism for the formation of a convex reach upstream of an active fault, which involves the migration of successive knickpoints that are generated by slip on the fault in individual earthquakes or clusters of earthquakes.

Finally, this study demonstrates that to understand and predict river incision across an actively growing normal fault we require not only a description of the fluvial incision process; we must also take into account the fact that empirically established scaling relationships between drainage area, high flow channel width and downstream distance may break down in this setting. Catchment geometry and channel network characteristics are strongly influenced by the three-dimensional uplift field around the growing fault segments in a way that can be readily understood (see conclusion 1 above). In contrast, the fundamental physical controls on hydraulic geometry in bedrock channels are less well understood (cf. Stark, 2006), particularly in areas of active tectonic uplift (cf. Wobus *et al.*, 2006). Resolving this issue must remain an outstanding research objective.

## APPENDIX A – Physical interpretation of fluvial length-scale $L_f$

Foster & Meyer (1971) hypothesised that the rate of detachment of cohesive material by overland flow depends on hydrodynamic shear and on the relative flux of sediment in transport. Reasoning that available flow energy will tend to be partitioned between sediment transport and particle detachment, they proposed that the following is a conserved quantity:

$$\frac{D}{D_c} + \frac{q_s}{q_c} = 1 \quad (\text{A.1})$$

where  $D$  is detachment rate (with dimensions  $L/T$ ),  $D_c$  is detachment capacity under clear-water flow,  $q_s$  is sediment transport rate per unit flow width (with dimensions  $L^2/T$ ) and  $q_c$  is sediment transport capacity per unit flow width (with units  $L^2/T$ ). Equation (A.1) describes a system in which sediment transport inhibits net particle detachment through effects such as partial shielding of the bed, re-attachment of cohesive aggregates, and damping of near-bed fluid momentum. The formulation assumes negligible enhancement of detachment by sediment flux through, for example, energetic particle impacts.

Rearranging (A.1) to solve for detachment rate we obtain

$$D = D_c(1 - q_s/q_c). \quad (\text{A.2})$$

With a slight rearrangement, Eqn. (A.2) can be written in the same form as a first-order chemical reaction, in which the rate of detachment depends on the difference between sediment flux (analogous to concentration) and transport capacity (analogous to equilibrium concentration):

$$D = \frac{dq_s}{dx} = \frac{D_c}{q_c}(q_c - q_s). \quad (\text{A.3})$$

The first factor on the right-hand side of (A.3),  $D_c/q_c$ , has dimensions of inverse length, and physically represents the distance over which, for constant  $q_c$  and  $D_c$ , the ratio  $q_s/q_c$  increases by 1*e* (see also Beaumont *et al.*, 1992). Equation (A.3) can also be written in terms of volumetric flux and capacity,  $Q_s$  and  $Q_c$ , respectively:

$$D = \frac{1}{W} \frac{D_c}{q_c}(Q_c - Q_s) \quad (\text{A.4})$$

where  $Q_s = Wq_s$  and  $Q_c = Wq_c$ . Comparing Eqn. (A.4) with the revised formulation of the ‘under-capacity’ model (van der Beek & Bishop, 2003), i.e.

$$\frac{dh}{dt} = \frac{1}{W} \frac{1}{L_f}(Q_c - Q_s). \quad (\text{A.5})$$

It is clear that they are identical if  $L_f = q_c/D_c$ . Both expressions are dimensionally consistent with  $L_f$  having units of length. Thus  $L_f$  can *either* be thought of as a length scale (as explained above) *or* as the ratio of transport capacity ( $q_c$ ) to detachment capacity ( $D_c$ ). High values of  $L_f$  represent the case where the transport capacity of a river is

high compared with its detachment capacity ( $q_c \gg D_c$ ; resistant lithologies), so the river is strongly undersupplied ( $Q_s \ll Q_c$ ). Low values of  $L_f$  represent the case where the transport capacity is low compared with its detachment capacity ( $q_c \ll D_c$ ; erodible lithologies), so the river approaches its equilibrium carrying capacity ( $Q_s \approx Q_c$ ). Thus we can also think of  $L_f$  as the probability of particle detachment per unit length of downstream movement of a water parcel: high  $L_f$  represents a low probability, whereas low  $L_f$  represents a high probability.

The parameter  $L_f$  can be expressed in terms of other fluvial transport parameters by substituting expressions for  $q_c$  and  $D_c$  and deriving  $L_f = q_c/D_c$ . Volumetric transport capacity in the fluvial incision model used in this study is given by

$$Q_c = K_f Q S \quad (\text{A.6})$$

where  $K_f$  is a dimensionless constant. Thus

$$q_c = Q_c/W = K_f(Q/W)S. \quad (\text{A.7})$$

Thus, the transport capacity is assumed to scale with stream power per unit bed area, as predicted by several common bedload transport formulas (e.g. Meyer-Peter & Müller, 1948). Foster & Meyer (1971), Stein *et al.* (1993), and Howard (1994), among others, conjectured that clear-water detachment capacity is a function of boundary shear stress,  $\tau$ , over and above a threshold value:

$$D_c = K_d(\tau - \tau_c)^\xi, \tau > \tau_c \quad (\text{A.8})$$

where  $K_d$  is a dimensional constant with dimensions implied by the above equation. We assume that detachment capacity depends on unit stream power, so that the exponent  $\xi = 3/2$  in Eqn. (A.8) (Seidl & Dietrich, 1992; Howard, 1994; Whipple & Tucker, 1999). Under steady, uniform flow, cross-section average boundary shear stress depends on unit flow ( $q$ ), gradient ( $S$ ), and roughness. It is well approximated by

$$\tau = K_t(Q/W)^{2/3} S^{2/3} \quad (\text{A.9})$$

where  $K_t$  is a dimensional constant with dimensions implied by the above equation. Implicit in the fluvial incision model used here is the assumption that  $\tau_c \approx 0$ . Strictly speaking, this assumption implies that the bedrock contains some fraction (possibly small) of friable material that is readily entrained. Such an assumption places constraints on the predicted morphodynamics (Tucker, 2004). Combining Eqns (A.8) and (A.9) we obtain

$$D_c = K_2(Q/W) S \quad (\text{A.10})$$

where the constant  $K_2$  has dimensions of  $L^{-1}$ . Thus

$$L_f = \frac{q_c}{D_c} = \frac{K_f}{K_2}. \quad (\text{A.11})$$

The parameters  $K_f$  and  $K_2$  depend primarily on the properties of the eroding substrate although  $K_2$  also depends on channel roughness.

## ACKNOWLEDGEMENTS

This work was supported by NERC Research Grants NE/B504165/1 (Cowie, Roberts, Attal, Tucker), NER/S/A/2002/10359 (A. Whittaker), EPSRC Grant Gr/T11753/01 (M. Naylor), and ARO Grant 47033EV (G. Tucker). P. Cowie was also partially supported by a Royal Society of London University Research Fellowship. Peter van der Beek helped in the initial implementation of the code CASCADE used in this study. The idea for this paper originated from stimulating discussions with Ruth Gilpin. Useful comments and reviews from Alex Densmore, Sanjeev Gupta Noah Snyder and Greg Mack improved the manuscript. Several figures were prepared using GMT software (Wessel & Smith, 1998)

## REFERENCES

- ALLEN, P.A. & DENSMORE, A.L. (2000) Sediment flux from an uplifting fault block. *Basin Res.*, **12**, 367–380.
- BEAUMONT, C., FULLSACK, P. & HAMILTON, J. (1992) Erosional control of active compressional orogens. In: *Thrust Tectonics* (Ed. by K.R. McClay), pp. 1–18. Chapman & Hall, New York.
- BRAUN, J. & SAMBRIDGE, M. (1997) Modelling landscape evolution on geological timescales: a new method based on irregular spatial discretization. *Basin Res.*, **9**, 27–52.
- BULL, J.M., BARNES, P.M., LAMARCHE, G., SANDERSON, D.J., COWIE, P.A., TAYLOR, S.K. & DIX, J.K. (2006) High-resolution record of displacement accumulation on an active normal fault: implications for models of slip accumulation during repeated earthquakes. *J. Struct. Geol.*, **28**(7), 1146–1166.
- BURBANK, D.W. & ANDERSON, R.S. (2001) *Tectonic Geomorphology*. Blackwell Science, Oxford.
- CARRETIER, S. & LUCAZEAU, F. (2005) How does alluvial sedimentation at range fronts modify the erosional dynamics of mountain catchments? *Basin Res.*, **17**, 361–382.
- CHAMPEL, B., VAN DER BEEK, P., MUGNIER, J.L. & LETURMY, P. (2002) Growth and lateral propagation of fault-related folds in the Siwaliks of western Nepal: rates, mechanisms, and geomorphic signature. *J. Geophys. Res.*, **107**, 2111.
- CHEVALIER, M.-L., RYERSON, F.J., TAPPONNIER, P., FINKEL, R.C., VAN DER WOERD, J., HAIBING, L. & QING, L. (2005) Slip-rate measurements on the Karakorum fault may imply secular variations in fault motion. *Science*, **307**, 411–414.
- CONTRERAS, J., ANDERS, M.H. & SCHOLZ, C.H. (2000) Growth of a normal fault system: observations from the Lake Malawi basin of the East Africa rift system. *J. Struct. Geol.*, **22**, 159–168.
- COWIE, P.A. (1998) A healing-reloading feedback control on the growth rate of seismogenic faults. *J. Struct. Geol.*, **20**, 1075–1087.
- COWIE, P.A., GUPTA, S. & DAWERS, N.H. (2000) Implications of fault interaction for early syn-rift sedimentation: insights from a numerical fault growth model. *Basin Res.*, **12**, 241–262.
- COWIE, P.A. & ROBERTS, G.P. (2001) Constraining slip rates and spacings of active normal faults. *J. Struct. Geol.*, **23**, 1901–1903.
- COWIE, P.A., UNDERHILL, J.R., BEHN, M.D., LIN, J. & GILL, C. (2005) Spatio-temporal evolution of strain accumulation derived from multi-scale observations of Late Jurassic rifting in the northern North Sea: a critical evaluation of models for lithospheric extension. *Earth Planet Sci. Lett.*, **234**, 401–419.
- COWIE, P.A., VANNESTE, C. & SORNETTE, D. (1993) Statistical physics model for the spatio-temporal evolution of faults. *J. Geophys. Res.*, **98**, 21809–21822.
- DAWERS, N.H. & ANDERS, M. (1995) Displacement-length scaling and fault linkage. *J. Structural Geology*, **17**, 604–614.
- DENSMORE, A.L., DAWERS, N.H., GUPTA, S., ALLEN, P.A. & GILPIN, R. (2003) Landscape evolution at extensional relay zones. *J. Geophys. Res.*, **108**, 2273, doi:10.1029/2001JB001741.
- DENSMORE, A.L., DAWERS, N.H., GUPTA, S., GUIDON, R. & GOLDIN, T. (2004) Footwall topographic development during continental extension. *J. Geophys. Res. Earth Surf.*, **109**, F03001.
- DENSMORE, A., ELLIS, M. & ANDERSON, R. (1998) Landsliding and the evolution of normal-fault-bounded mountains. *J. Geophys. Res.*, **103**, 15203–15219.
- DORSEY, R.J. & ROERING, J.J. (2006) Quaternary landscape evolution in the San Jacinto fault zone, Peninsular Ranges of Southern California: transient response to strike-slip fault initiation. *Geomorphology*, **73**, 16–32.
- DUVALL, A., KIRBY, E. & BURBANK, D. (2004) Tectonic and lithologic controls on bedrock channel profiles and processes in coastal California. *J. Geophys. Res.*, **109**, F03002, doi:10.1029/2003JF000086.
- ELIET, P.P. & GAWTHORPE, R.L. (1995) Drainage development and sediment supply within rifts, examples from the Sperchios basin, mainland Greece. *J. Geol. Soc. Lond.*, **152**, 883–893.
- FINNEGAN, N.J., ROE, G., MONTGOMERY, D. & HALLET, B. (2005) Controls on the channel width of rivers: implications for modelling fluvial incision of bedrock. *Geology*, **33**, 229–232.
- FOSTER, G.R. & MEYER, L.D. (1971) A closed-form soil erosion equation for upland areas. In: *Sedimentation* (Ed. by H.W. Shen), pp. 12.1–12.19. Department of Civil Engineering, Colorado State University, Fort Collins.
- FRIEDRICH, A.M., WERNICKE, B.P., NIEMI, N.A., BENNETT, R.A. & DAVIS, J.L. (2003) Comparison of geologic and geodetic data from the Wasatch region, Utah and implications for the spectral character of Earth deformation at periods of 10 to 10 million years. *J. Geophys. Res.*, **108**, 2109, doi:10.1029/2001JB000682.
- GANAS, A. (1997) Fault segmentation and seismic hazard assessment in the Gulf of Evia Rift, central Greece. Unpublished. PhD Thesis, University of Reading, 369 pages.
- GASPARINI, N., BRAS, R.L. & WHIPPLE, K.X. (2006) Numerical modeling of non-steady-state river profile evolution using a sediment-flux-dependent erosion incision model. In: *Tectonics, Climate, and Landscape Evolution* (Ed. by S.D. Willett, N. Hovius, M.T. Brandon & D.M. Fisher), *Geol. Soc. Am. Spec. Paper*, **398**, 127–141.
- GAWTHORPE, R.L. & HURST, J.M. (1993) Transfer zones in extensional basins – their structural style and influence on drainage development and stratigraphy. *J. Geol. Soc.*, **150**, 1137–1152.
- GAWTHORPE, R.L., JACKSON, C.A.L., YOUNG, M.J., SHARP, I.R., MOUSTAFA, A.R. & LEPPARD, C.W. (2003) Normal fault growth, displacement localisation and the evolution of normal fault populations: the Hammam Faraun fault block, Suez Rift, Egypt. *J. Struct. Geol.*, **25**, 1347–1348.
- GAWTHORPE, R.L. & LEEDER, M.R. (2000) Tectono-sedimentary evolution of active extensional basins. *Basin Res.*, **12**, 195–218.

- GILPIN, R.E. (2003) Interaction between stream development and propagating normal faults. PhD Thesis, University of Edinburgh.
- GOLDSWORTHY, M. & JACKSON, J. (2001) Migration of activity within normal fault systems: examples from the Quaternary of mainland Greece. *J. Struct. Geol.*, **23**, 489–506.
- GUPTA, S. & COWIE, P.A. (2000) Processes and controls in the stratigraphic development of extensional basins. *Basin Res.*, **12**, 185–194.
- GUPTA, S., COWIE, P.A., DAWERS, N.H. & UNDERHILL, J.R. (1998) A mechanism to explain rift-basin subsidence and stratigraphic patterns through fault array evolution. *Geology*, **26**, 595–598.
- GUPTA, S., UNDERHILL, J.R., SHARP, I.R. & GAWTHORPE, R.L. (1999) Role of fault interaction in controlling synrift dispersal patterns: Miocene, Abu Alaqa Group, Suez Rift, Sinai, Egypt. *Basin Res.*, **11**, 167–189.
- HARBOR, D.J. (1998) Dynamic equilibrium between an active uplift and the Sevier River, Utah. *J. Geol.*, **106**, 181–194.
- HARDY, S. & GAWTHORPE, R. (2002) Normal fault control on bedrock channel incision and sediment supply: insights from numerical modelling. *J. Geophys. Res.*, **107**, 2246, doi: 10.1029/2001JB000166.
- HOWARD, A.D. (1994) A detachment-limited model of drainage basin evolution. *Water Res. Res.*, **30**, 2261–2285.
- JACKSON, C.A.L., GAWTHORPE, R.L. & SHARP, I.R. (2002) Growth and linkage of the East Tanka fault zone, Suez rift: structural style and syn-rift stratigraphic response. *J. Geol. Soc.*, **159**, 175–187.
- KIRBY, E. & WHIPPLE, K. (2001) Quantifying differential rock-uplift rates via stream profile analysis. *Geology*, **29**(5), 415–418.
- KOOI, H. & BEAUMONT, C. (1996) Large-scale geomorphology: classical concepts reconciled and integrated with contemporary ideas via a surface processes model. *J. Geophys. Res.*, **101**, 3361–3386.
- LAMBIASE, J.J. & BOSWORTH, W. (1995) Structural controls on sedimentation in continental rifts. In: *Hydrocarbon Habitat in Rift Basins* (Ed. by J.J. Lambiase). *Spec. Publ. Geol. Soc. Lond.*, **80**, 117–144.
- LAVÉ, J. & AVOUAC, J.P. (2001) Fluvial incision and tectonic uplift across the Himalaya of central Nepal. *J. Geophys. Res.*, **106**, 26561–26591.
- LEEDER, M.R. & JACKSON, J. (1993) Interaction between normal faulting and drainage in active extensional basins, with examples from western United States and Mainland Greece. *Basin Res.*, **5**, 79–102.
- LEOPOLD, L.B. & MADDOCK, T. Jr. (1953). The hydraulic geometry of stream channels and some physiographic implications. U.S. Geological Survey Professional Paper, 252, Washington, DC.
- MCLEOD, A., DAWERS, N.H. & UNDERHILL, J.R. (2000) The propagation and linkage of normal faults: insights from the Strathspey-Brent-Statfjord fault array, Northern North Sea. *Basin Res.*, **12**, 263–284.
- MEYER-PETER, E. & MÜLLER, R. (1948) *Formulas for bedload transport. Proceedings, 2nd IAHR Congress*, Stockholm, Sweden.
- MONTGOMERY, D.R. & GRAN, K.B. (2001) Downstream variations in the width of bedrock channels. *Water Res.*, **37**, 1841–1846.
- MORTIMER, E.J., GUPTA, S. & COWIE, P.A. (2005) Clinof orm nucleation and growth in coarse-grained deltas, Loreto Basin, Baja California Sur, Mexico: a response to episodic accelerations in fault displacement. *Basin Res.*, **17**, 337–359.
- OLLIER, C.D. (1981) *Tectonics and Landforms*. Longman, London.
- PALUMBO, L., BENEDETTI, L., BOURLÈS, D., CINQUE, A. & FINKEL, R. (2004) Slip history of the Magnola fault (Apennines, Central Italy) from <sup>36</sup>Cl surface exposure dating: evidence for strong earthquakes over the Holocene. *E. Planet. Sci. Lett.*, **225**, 163–176.
- PROSSER, S. (1993) Rift-related linked depositional systems and their seismic expression. In: *Tectonics and Seismic Sequence Stratigraphy* (Ed. by G.D. Williams & A. Dobbs), *Spec. Publ. Geol. Soc. Lond.*, **71**, 35–66.
- ROBERTS, S. & JACKSON, J. (1991) Active normal faulting in mainland Greece: an overview. In: *The Geometry of Normal Faults* (Ed. by A.M. Roberts, G. Yielding & B. Freeman), *Geol. Soc. Lond. Spec. Publ.* **56**, 125–142.
- ROBERTS, G.P. & MICHETTI, A.M. (2004) Spatial and temporal variations in growth rates along active normal fault systems: an example from the Lazio-Abruzzo Apennines, central Italy. *J. Struct. Geol.*, **26**, 339–376.
- ROBERTS, G.P., MICHETTI, A., COWIE, P.A., MOREWOOD, N.C. & PAPANIKOLAOU, I. (2002) Fault slip-rate variations during crustal-scale strain localisation, Central Italy. *Geophys. Res. Lett.*, **29**(8), 10.1029/2001GL013529.
- ROCKWELL, T.K., LINDVALL, S., HERZBERG, M., MURBACH, D., DAWSON, T. & BERGER, G. (2000) Paleoseismology of the Johnson Valley, Kickapoo, and Homestead Valley faults: clustering of earthquakes in the Eastern California shear zone. *Bull. Seism. Soc. Am.*, **90**, 1200–1236.
- SEIDL, M. & DIETRICH, W.E. (1992) The problem of channel erosion into bedrock. *Catena Suppl.*, **23**, 101–124.
- SHARP, I.R., GAWTHORPE, R.L., ARMSTRONG, B. & UNDERHILL, J.R. (2000) Propagation history and passive rotation of mesoscale normal faults: implications for synrift stratigraphic development. *Basin Res.*, **12**, 285–306.
- SKLAR, L. & DIETRICH, W.E. (1998) River longitudinal profiles and bedrock incision models: stream power and the influence of sediment supply. In: *Rivers Over Rock: Fluvial Processes in Bedrock Channels* (Ed. by E. Wohl & K. Tinkler), *Geophys. Monogr. Ser.*, **107**, 237–260. AGU, Washington, D.C.
- SKLAR, L. & DIETRICH, W.E. (2004) A mechanistic model for river incision into bedrock by saltating bedload. *Water Res. Res.*, **40**, W06301, doi:10.1029/2003WR002496.
- SNYDER, N.P., WHIPPLE, K.X., TUCKER, G.E. & MERRITTS, D.J. (2000) Landscape response to tectonic forcing: digital elevation model analysis of stream profiles in the Mendocino triple junction region, northern California. *Bull. Geol. Soc. Am.*, **112**, 1250–1263.
- SNYDER, N.P., WHIPPLE, K.X., TUCKER, G.E. & MERRITTS, D.J. (2003) Channel response to tectonic forcing: field analysis of stream morphology and hydrology in the Mendocino triple junction region, northern California. *Geomorphology*, **53**, 97–127.
- SORNETTE, D., MILTENBERGER, P. & VANNESTE, C. (1994) Statistical physics of fault patterns self-organised by repeated earthquakes. *Pure Appl. Geophys.*, **142**, 491–527.
- STARK, C.P. (2006) A self-regulating model of bedrock river channel geometry. *Geophys. Res. Lett.*, **33**, L04402.
- STEIN, O.R., JULIEN, P.Y. & ALONSO, C.V. (1993) Mechanics of jet scour downstream of a headcut. *J. Hydraul. Res. IAHR*, **31**(6), 723–738.
- SÓLYOM, P. & TUCKER, G.E. (2004) Effect of limited storm duration on landscape evolution, drainage basin geometry and hydrograph shapes. *J. Geophys. Res.*, **109**, F03012.

- TAYLOR, S.K., BULL, J.M., LAMARCHE, G. & BARNES, P.M. (2004) Normal fault growth and linkage in the Whakatane Graben, New Zealand, during the last 1.3 Myr. *J. Geophys. Res.*, **109**, B02408.
- TRUDGILL, B.D. (2002) Structural controls on drainage development in the Canyonlands grabens of southeast Utah. *AAPG Bull.*, **86**, 1095–1112.
- TUCKER, G.E. (2004) Drainage basin sensitivity to tectonic and climatic forcing: implications of a stochastic model for the role of entrainment and erosion thresholds. *Earth Surf. Process. Landforms*, **29**, 185–205.
- TUCKER, G.E. & SLINGERLAND, R. (1996) Predicting sediment flux from fold and thrust belts. *Basin Res.*, **8**, 329–349.
- TUCKER, G.E. & WHIPPLE, K.X. (2002) Topographic outcomes predicted by stream erosion models: sensitivity analysis and intermodel comparison. *J. Geophys. Res.*, **107**, 2179, doi: 10.1029/2001JB000162.
- VAN DER BEEK, P. & BISHOP, P. (2003) Cenozoic river profile development in the Upper Lachlan catchment (SE Australia) as a test of quantitative fluvial incision models. *J. Geophys. Res.*, **108**, 2309.
- VAN DER BEEK, P. & BRAUN, J. (1998) Numerical modelling of landscape evolution on geological time-scales: a parameter analysis and comparison with the south-eastern highlands of Australia. *Basin Res.*, **10**, 49–68.
- VAN DER BEEK, P., CHAMPEL, B. & MUGNIER, J.L. (2002) Controls on drainage development in regions of active fault-propagation folding. *Geology*, **30**, 471–474.
- WESSEL, P. & SMITH, W.H.F. (1998) New, improved version of the Generic Mapping Tools released. *EOS Trans. Am. Geophys. Un.*, **79**, 579.
- WHIPPLE, K.X. & TRAYLER, G.E. (1996) Tectonic control of fan size: the importance of spatially variable subsidence rates. *Basin Res.*, **8**, 351–366.
- WHIPPLE, K.X. & TUCKER, G.E. (1999) Dynamics of the stream power river incision model: implications for height limits of mountain ranges, landscape response timescales and research needs. *J. Geophys. Res.*, **104**, 17661–17674.
- WHIPPLE, K.X. & TUCKER, G.E. (2002) Implications of sediment-flux-dependent river incision models for landscape evolution. *J. Geophys. Res.*, **107**, 2179, doi: 10.1029/2000JB000044.
- WHITTAKER, A.C., COWIE, P.A., ATTAL, M., TUCKER, G.E. & ROBERTS, G.P. (2006) Bedrock channel adjustment to tectonic forcing: Implications for predicting river incision rates. *Geology*, in press.
- WOBUS, C.W., TUCKER, G.E. & ANDERSON, R.S. (2006). Self-formed bedrock channels. *Geophys. Res. Lett.*, in press.
- WOHL, E. (2004) Limits of downstream hydraulic geometry. *Geology*, **32**, 897–900.

*Manuscript received 15 November 2005; Manuscript accepted 9 February 2006.*